Incorporating an iterative energy restraint for the Surface Energy Balance System (SEBS)

Evan Webster[a,c], Daniel Ramp[a,b], Richard T. Kingsford[a]

[a] *Centre for Ecosystem Science, School of Biological, Earth and Environmental Sciences, University of New South Wales, Sydney 2052 NSW, Australia*

[b] *School of Life Sciences, University of Technology Sydney, Broadway 2007 NSW, Australia*

[c] *Corresponding Author: Evan Webster, Centre for Ecosystem Science, School of Biological, Earth and Environmental Sciences, University of New South Wales, Sydney 2052 NSW, Australia, ph: +61293858295, f: +61293851558, e: e.webster@unsw.edu.au*

Keywords: Evapotranspiration, South-east Australia, Landsat, Surface Energy Balance, Surface Energy Balance System, Penman-Monteith, Triangular Energy Restraint

Abstract

The Surface Energy Balance System (SEBS) has proven itself as an effective remotely sensed estimator of actual evapotranspiration (ET_a). However, it has several vulnerabilities associated with the partitioning of the available energy (AE) at the land surface. We introduce a two stage energy restraint process into the SEBS algorithm (SEBS-ER) to overcome these vulnerabilities. The first offsets the remotely sensed surface temperature to ensure the surface to air temperature difference reflects AE, while the second stage uses a domain based image search process to identify and adjust the proportions of sensible (H) and latent (λE) heat flux with respect to AE. We effectively implemented SEBS-ER over 61 acquisitions over two Landsat tiles (path 90 row 84 and path 91 row 85) in south-eastern Australia that feature heterogeneous land covers. Across the two areas we showed that the SEBS-ER algorithm has: greater resilience to perturbed errors in surface energy balance algorithm inputs; significantly improved accuracy ($p<0.05$) at two eddy covariance flux towers in heavily forested (RMSE 62.3 $W\ m^{-2}$, R^2 0.879) and sub-alpine grassland (RMSE 33.2 $W\ m^{-2}$, R^2 0.939) land covers; and greater temporal stability across 52 daily actual evapotranspiration (ET_a) estimates compared to a temporally stable and independent ET_a dataset. The energy restraint within SEBS-ER has reduced exposure to the complex errors and uncertainties within remotely sensed, meteorological, and land type SEBS inputs, providing more reliable and accurate spatially distributed ET_a products.

1. Introduction

Evapotranspiration (ET) is a critical process for water accounting in catchment areas (Glenn et al., 2011), driving current and future water yields for urban populations (Chiew and McMahon, 2002; McVicar et al., 2012). It represents complex interactions involving moisture availability and transpiration, influenced by wind, temperature, heat fluxes, and surface roughness (Kalma et al., 2008). Estimating actual evapotranspiration (ET_a) and understanding how it varies spatially and temporally is essential for quantifying water loss across complex heterogeneous catchments (Glenn et al., 2011). Water planning authorities often rely on ET_a measurements from a few isolated ground flux towers or calculations of potential evapotranspiration (ET_o) (Monteith, 1965; Priestley and Taylor, 1972) or reference evapotranspiration (ET_r) (Allen et al., 1998) from one or more nearby meteorological ground stations. Estimations of catchment evaporative water loss and water yield are also complicated by patchy or non existent stream flow records (Winsemius et al., 2009), arising from substantial infrastructure costs or logistical difficulties. So, water accounting through hydrological models is often limited by the reliance on incomplete datasets (Merz et al., 2011; Winsemius et al., 2009), including relatively poor estimation of ET_a and ET_o. Satellite remote sensing techniques can reduce uncertainty within these inputs in hydrological models (Immerzeel and Droogers, 2008; Yin et al., 2016) through estimations of fine scale spatially explicit ET_a throughout catchments, improving water accounting for urban populations.

Remotely sensed thermal imagery and its estimation of surface temperature (T_S, K) is a critical component in surface energy balance (SEB) algorithms (Evett et al., 2012; Kalma et al., 2008) for the calculation of spatially explicit ET_a at landscape ($\approx$30 m) or regional (250 m - 1 km) scales. While spaceborne instruments like the Advanced Very High Resolution Radiometer (AVHRR) and the Moderate resolution Imaging Spectrometer (MODIS) can provide provide high temporal frequency ET_a assessments at regional, continental, or global scales (Kalma et al., 2008; Mu et al., 2011), significant ET_a variability is often present in agricultural or forested landscapes at a few hundred meters or less (Anderson et al., 2012). Landsat data are an obvious choice to obtain moderate spatial resolution (30m - 120m) SEB ET_a estimates, given continued investment in the Landsat program (Roy et al., 2014) combined with access to processed and freely available historical archives of thermal, near infrared and visible imagery (Masek et al., 2006). Moving forwards, Landsat 8 (Feb. 2013 onwards, Roy et al., 2014) and Sentinel 3 (Feb. 2016 onwards, Donlon et al., 2012) data will provide the basis for current and future moderate spatial resolution (10 m - 90 m) cost-free

SEB applications.

Over about 30 years of development (Carlson, 1986), different SEB algorithms now exist, such as the Surface Energy Balance System (SEBS) (Su, 2002), the Simplified Surface Energy Balance Index (S-SEBI) (Roerink et al., 2000), the Hybrid Dual-Source Scheme and Trapezoid Framework-Based Evapotranspiration Model (HTEM) (Yang and Shang, 2013), Mapping Evapotranspiration at High Resolution with Internalised Calibration (METRIC) (Allen et al., 2007), and others (Kustas and Norman, 1997; Long and Singh, 2012; Wang et al., 2014). Commonly, each algorithm employs a mechanism to constrain or reference sensible heat flux (H, $W\,m^{-2}$) and latent heat flux (λE, $W\,m^{-2}$) to the energy available at the land surface (AE); net radiation (R_N, $W\,m^{-2}$) minus soil heat flux (G, $W\,m^{-2}$). While the instantaneous sum of sensible and latent heat fluxes is not necessarily equal to AE due to regional advection effects, its imbalance can be mitigated when ET_a is quantified over daily time scales or longer (Allen et al., 2011a).

Within SEB models, the scaling or calibration of H and λE is critical to ensure the surface energy balance can be satisfied (Kalma et al., 2008), for individual remotely sensed land units. Triangular (Gampe et al., 2016; Knipper et al., 2016; Petropoulos et al., 2009a) or trapezoidal (Long and Singh, 2012) techniques are distinct in their approach for the constraint and partitioning of H and λE within SEB algorithms. They generally exploit the relationship between T_S and a measure or index of vegetation (T_S-VI) (Carlson, 2007; Long et al., 2012; Price, 1990) to define boundaries or vertices associated with theoretical conditions of the surface energy balance. They have considerable utility and applicability over different environments and landscape scales, particularly those with limited ground reference data where there are often water management challenges (Gampe et al., 2016; Long et al., 2012).

Approaches vary for the choice of the vegetative axis, with most using the Normalised Difference Vegetation Index ($NDVI$) (Han et al., 2006; Sun, 2016; Yang and Shang, 2013), the fractional vegetation cover (Carlson, 2007), or the Leaf Area Index (LAI) (Han et al., 2006), while use of T_S among existing ET triangle methods remains similar, apart from incorporating the difference to air temperature (T_A, $^{\circ}C$) (Long and Singh, 2012). Automated detection or definition of triangle/trapezoidal boundaries and vertices is a crucial requirement for the fast and objective production of ET_a, particularly for deriving estimates over large areas (Elhaddad and Garcia, 2014) and dense time series.

T_S-VI triangle and trapezoidal models have performed well when compared to other

forms of energy restraint (Lian and Huang, 2016; Long and Singh, 2013) and when validated against Large Aperture Scintillometers (LAS) (Tang et al., 2010) or eddy covariance flux towers (Long and Singh, 2012; Long et al., 2012). However, T_S-VI techniques are often limited to heterogeneous areas that exhibit different vegetation conditions, varying across a range of water availabilities (Long et al., 2012). Also, as the domain size and land unit resolution changes, T_S-VI boundaries or vertices may vary (Long et al., 2012) and questions remain as to whether a triangle or a trapezoidal theoretical structure better encompasses the complete range of T_S-VI values (Long et al., 2012), and at what areal scale triangle techniques can be successfully implemented (Long et al., 2012).

SEBS uniquely applies the Penman-Monteith combination equation (Monteith, 1965) to determine the residual H (H_{wet}, $W\,m^{-2}$) for conditions where λE reaches the upper potential rate (λE_{wet}, $W\,m^{-2}$) (Su, 2002), different to most SEB algorithms (Kalma et al., 2008). This removes a common evaporative energy control at the cold and wet limit common among many SEB algorithms, that λE_{wet} is equivalent to AE (Bastiaanssen et al., 1998; Long and Singh, 2012; Yang and Shang, 2013). The METRIC algorithm also applies a similar evaporative control (Allen et al., 2007), however, it relies on the identification of representative land units relevant to ET_r surface conditions (Allen et al., 2013). Comparatively, the determination of $H_{wet}/\lambda E_{wet}$ by SEBS is spatially explicit and is not restricted by the need to identify specific land units. This makes SEBS more applicable to the estimation of ET_a over non-agricultural land types, where the composition of plant and tree species can be heterogeneous and is often largely unknown.

McCabe and Wood (2006) reported consistent flux estimates between different satellite platforms and at different spatial scales, indicating SEBS has good utility to create multi-scale high spatial and temporal resolution ET_a datasets, useful for hydrological accounting. When SEBS has been compared to other SEB algorithms it has been show to perform well. Tang et al. (2011) found comparable performance to the Two-Source Energy Balance (TSEB) model and improved performance to a T_S-VI triangle technique over wheat and corn agricultural land types. Yang and Shang (2013) obtained a root mean squared error (RMSE) for SEBS slightly larger than that for HTEM in wheat and corn, and Webster et al. (2016) showed SEBS had lower RMSE compared to S-SEBI and HTEM in forested and sub-alpine grassland land types. Furthermore, the current implementation of SEBS contains some structural limitations that if addressed may further improve its performance and applicability across different land types.

SEBS's constraint of H is different from other SEB algorithms; the initial unbounded estimates of H and H_{wet} are used directly to calculate evaporative fraction (Λ) (Su, 2002). While H_{wet} can not exceed AE, there is no current control to enforce H to be greater than H_{wet} or less than AE (Su, 2002). This makes SEBS vulnerable to errors and bias within input variables related to the determination of H and H_{wet} (Liaqat and Choi, 2015). These error sources include: the interpolative uncertainty in the calculation of T_A, wind speed (U_x, $m\ s^{-1}$), vapour pressure (P_{vap}, kPa), and solar exposure (δ, $MJ\ day^{-1}$) (Elhag, 2016; Webster et al., 2016); errors and bias in T_S associated with the atmospheric correction for atmospheric transmissivity (τ), upwelling path radiance (R_{path}) and downwelling sky radiance (R_{sky}) (Allen et al., 2011a); landscape heterogeneity (Gibson et al., 2011; Rwasoka et al., 2011); and the uncertainty in vegetation fraction and σ_s given the absence of accurate land type classifications (Gibson et al., 2011). For example, SEBS was significantly more sensitive to errors in T_S and leaf area index (LAI) inputs compared to TSEB (Tang et al., 2011). Furthermore, Timmermans et al. (2013) used the Soil Canopy Observation, Photochemistry and Energy fluxes (SCOPE) model to evaluate and validate SEBS by simulation of remote sensing input variables. They identified large uncertainties in SEBS G and H driven primarily by the original parametrisation for the roughness height for heat transfer (Z_{OH}, m) (Su, 2002), which was not suitable for tall canopies such as maize (Timmermans et al., 2013). After improving Z_{OH} using LAI to account for tall vegetation, H was still underestimated and λE overestimated (Timmermans et al., 2013). Also acknowledging the limitation in Z_{OH}, Gokmen et al. (2012) utilised microwave soil moisture measurements to account for increased water stress for Z_{OH} in the semi-arid Konya basin Turkey, improving estimations of SEBS flux components. Unfortunately, availability of supplementary microwave soil moisture measurements is often scarce in remote or heterogeneous environments (Daly, 2006).

The overall goal of this research was straightforward; to evaluate the effectiveness of adding a two dimensional (EVI - H) energy restraint process into the SEBS algorithm (SEBS-ER) to improve its operation, accuracy and temporal stability. Given the development task and the three performance aspects for algorithm improvement, we separated our research into four specific aims: a) to effectively integrate an energy restraint component into the original SEBS algorithm; b) to evaluate how this improved resilience to errors and bias in meteorological and remotely sensed inputs; c) to identify how this improved SEBS algorithm accuracy with respect to independent validation data; and d) to show that SEBS-ER improved the temporal stability of SEBS estimates over extended time frames and various

land types.

2. Background Theory

Below, we outline the execution of the existing SEBS process from Su (2002) specific to the determination of H and λE. The SEBS H and λE partitioning process starts with the definition of aerodynamic resistance (R_{AH}, $s\,m^{-1}$) (1). Su (2002) uses Monin-Obukhov (MO) stability correction functions for heat (Ψ_h) and momentum (Ψ_m) (Brutsaert, 1999) to define a single source estimate of R_{AH} between the ground and the Atmospheric Surface Layer (ASL) (1):

$$R_{AH} = \frac{\left[ln\frac{Z_h - D_0}{Z_{0H}} - \Psi_h\frac{Z_h - D_0}{L} + \Psi_h\frac{Z_{0H}}{L}\right]}{U_*\,k} \tag{1}$$

where k is von Karmen's constant (0.41), Z_{OH} is the roughness height for heat transport (m) referenced to the height of the air temperature observation (Z_h, m), and D_o is the zero plane displacement height (m). U_* is the friction velocity to momentum transport (2):

$$U_* = \frac{U_x\,k}{\left[ln\frac{Z_m - D_0}{Z_{0M}} - \Psi_m\frac{Z_m - D_0}{L} + \Psi_m\frac{Z_{0M}}{L}\right]} \tag{2}$$

within the ASL where Z_m is the height (m) of the wind speed observation (U_x, $m\,s^{-1}$), Z_{OM} is the roughness height for momentum transport (m), and L is the MO length (3, m).

$$L = -\frac{\rho\,C_p\,U_*^3\,T_V}{k\,g\,H} \tag{3}$$

Where ρ is the density of the air ($kg\,m^{-3}$), C_p is the specific heat constant for air (1012 $J\,kg^{-1}\,K^{-1}$), g is the gravitational constant (9.81 $m\,s^{-2}$), and T_V is the virtual temperature of the air (^oC). With R_{AH} estimated, SEBS derives H (4):

$$H = \frac{\rho\,C_p\,(T_S - T_A)}{R_{AH}} \tag{4}$$

and uses it to progressively adjust R_{AH} through L (3) via Ψ_m and Ψ_h until a stable solution is reached for H.

SEBS does not require that λE is equivalent to AE under conditions of maximum evaporation (λE_{wet}, $W\,m^{-2}$) (Su, 2002), rather it assumes H_{wet} and λE_{wet} sum to AE (5):

$$H_{wet} = R_N - G - \lambda E_{wet}. \tag{5}$$

Su (2002) estimates H_{wet} from an adaption of the Penman Monteith combination equation (Monteith, 1965) (6):

$$H_{wet} = \left((R_N - G) - \frac{\rho C_p}{R_{EW}}.\frac{P_{sat} - P_{vap}}{\gamma}\right) / \left(1 + \frac{\Delta}{\gamma}\right) \tag{6}$$

where P_{sat} is saturated vapour pressure (kPa), γ is the psychometric constant ($0.073\ kPa^{\circ}C^{-1}$), Δ is the slope of the saturation pressure curve and R_{EW} is the external resistance to heat transport (7, $s\ m^{-1}$) at λE_{wet}:

$$R_{EW} = \frac{1}{kU_*}\left[ln\left(\frac{Z_h - D_o}{Z_{0H}}\right) - \Psi_h\left(\frac{Z_h - D_o}{L_{wet}}\right) + \Psi_h\left(\frac{Z_{0H}}{L_{wet}}\right)\right]. \quad (7)$$

L_{wet} is the MO length at λE_{wet} (8, m):

$$L_{wet} = -\frac{\rho\, U_*^3}{k\, g\, 0.61(R_N - G)/\lambda} \quad (8)$$

and λ is the latent heat of vaporisation of water (2.26, $MJ\ kg^{-1}$).

Considering H_{wet}, Su (2002) defines the relative evaporative fraction (Λ_r) as (9):

$$\Lambda_r = 1 - \frac{H - H_{wet}}{R_N - G - H_{wet}} \quad (9)$$

to derive the evaporative fraction (Λ) (10):

$$\Lambda = \Lambda_r \frac{(R_N - G - H_{wet})}{R_N - G} \quad (10)$$

to determine λE from AE (11):

$$\lambda E = \Lambda_r(R_N - G - H_{wet}) = \Lambda(R_N - G). \quad (11)$$

3. Site Details and Data

3.1. Study Sites

Our research addressed the four objectives across two study areas represented by two Landsat image tiles (path 90 row 84 and path 91 row 85) (Fig. 1). The Canberra study area (37,648 km^2), represented by Landsat image tile path 91, row 85 in south-east Australia, featured agricultural and grazing land types in the north-west corner through to tall forested mixed eucalyptus forests (>40 m) and alpine grasslands (Keith, 2004) in the central and south-east extents. Modelled vegetation height (Scarth, 2014) varied across these land use types from 0.1 m in the agricultural and grazing areas through to 28 m in the forested regions (Fig. 1). Topography varied substantially around the Great Dividing Range, ranging from 2,228 m in the alpine areas to 41 m in the western agricultural areas (Fig. 1). Mean annual precipitation ranged from 2180 mm in the alpine areas along the Great Dividing Range to 520 mm in the far north-west corner of the study area (Fig. 1).

The Sydney study area (38,129 km^2), represented by Landsat image tile path 90, row 84 in south-east Australia, within one river basin, incorporated 16 catchment areas with

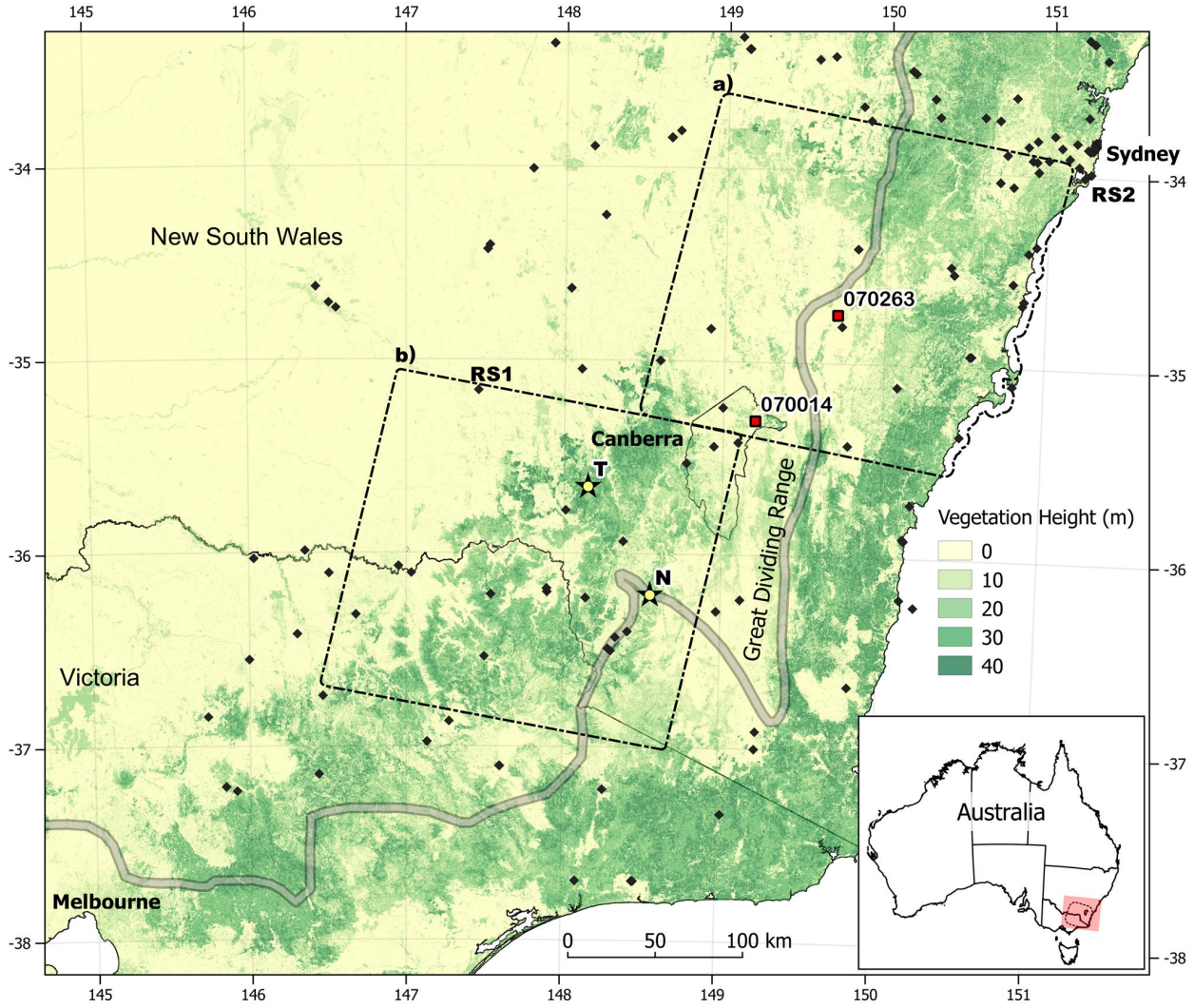

Figure 1: Two study areas in south-east Australia: a) the Sydney study area (Landsat tile (path 90, row 84)) contained two long term pan evaporation stations (squares with station IDs); and b) the Canberra study area (Landsat tile (path 91, row 85)), with the Tumbarumba (star T) and Nimmo High Plains (star N) eddy covariance flux towers. Dark grey diamonds were the meteorological ground stations used to source T_A, U_x, P_{vap}, and P_{air} meteorological inputs for SEBS and SEBS-ER. The RS1 annotation indicates the location of the Wagga Wagga radiosonde station and the RS2 annotation indicates the location of the Sydney International airport radiosonde station. Coloured Shading showed relative height of the vegetation across south east Australia (Scarth, 2014). The WGS 84 coordinate grid was overlaid on top of the map UTM 55N projection.

diverse topography and land types (Fig. 1). The Great Dividing Range ran through the centre (North to South) of the Sydney study area, partitioning coastal and inland meteorological processes (Fig. 1). We analysed data over about 10 years (1 Dec 1999 - 22 Mar 2010), including two large wildfires (2001 and 2007), many hazard reduction burns, heavy precipitation events and dry periods, creating a heterogeneous landscape with a dynamic range of ET_a values. Elevation extended from sea level through to 1593 m, with a large

plateau between 600-800 m to the east of the Great Dividing Range (Fig. 1). Modelled vegetation height (Scarth, 2014) ranged from 0.1 m in agricultural and grazing areas through to 28 m in the south-west corner of the study area (Fig. 1). Mean annual precipitation featured a distinct band between 600 - 900 mm extending to 1847 mm halfway along the eastern coastal boundary down to 617 mm within the northern limits of Australia's Capital Territory (ACT).

3.2. Input Data

Landsat 5 Thematic Mapper (TM) and Landsat 7 Enhanced Thematic Mapper (ETM+) surface reflectance and thermal data were used as the foundation for our analyses. Nine Landsat 5 TM acquisitions were obtained for the Canberra study area, all featuring less than 30% cloud contamination (Fig. 2a). Fifty-two acquisitions were obtained for the

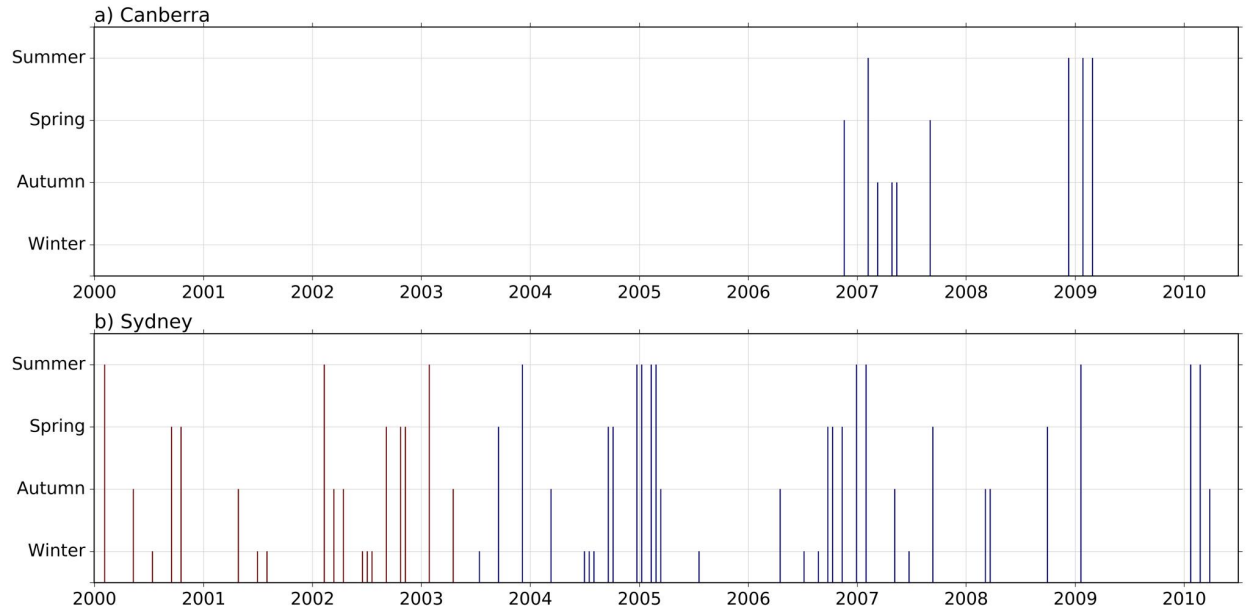

Figure 2: a) Nine Landsat acquisition dates for the Canberra study area (Fig. 1) were used to test the sensitivity, resilience and accuracy of the SEBS and SEBS-ER surface energy balance algorithms. All nine Landsat acquisitions were from the Landsat 5 Thematic Mapper (TM) (blue). b) Fifty-two Landsat acquisition dates for the Sydney study area (Fig. 1) were used to test the temporal stability of the SEBS and SEBS-ER surface energy balance algorithms. The Landsat data (1 Dec 1999 - 16 Apr 2003) were acquired by the Landsat 7 ETM+ (red) while Landsat data from 13 Jul 2003 onwards were acquired by the Landsat 5 TM (blue).Precise acquisition dates ca be found within the atmospheric correction tables located in Appendix A.

Sydney study area: 20 Landsat 7 ETM+ acquisitions (1 Dec 1999 - 16 Apr 2003) and 32 Landsat 5 acquisitions (13 Jul 2003 - 26 Mar 2010) (Fig. 2b). Given the limited number of Landsat 5 scenes in the period prior to its shutdown and the start of Landsat 8 operational

data (Feb 2013), no Landsat 8 data were used within the analysis. Details of the source and preprocessing of the multispectral, meteorological, topographic, and vegetation height data are outlined in Appendix A.

Within the Canberra study area, data from two eddy covariance flux towers were obtained from OzFlux (Leuning, 2002; Simpson, 2012) (Fig. 1), over the range of acquisition dates (Fig. 2a). The first tower was at Tumbarumba (Fig. 1), a 70 m high tower within a 40 m high wet sclerophyll forest. The second tower was on the Nimmo High Plains of the Monaro region (Fig. 1), in seasonally grazed sub-alpine grassland with a tower height of 2.5 m.

4. Methods

4.1. Implementation of the SEBS Energy Restraint

Daily and synoptic meteorological data were collated for each Landsat acquisition date, for each study area (Fig. 1). T_M and T_X data were temporally interpolated to T_A at the time of the Landsat acquisition using the TM method (Cesaraccio et al., 2001), while U_x, P_{air} and P_{vap} were linearly interpolated from previous and subsequent observations. Before spatial interpolation using Inverse Distance Weighting (IDW), the near surface elevation dependence (NSED) of T_A, U_x, P_{air}, P_{vap} and δ meteorological inputs were determined using radiosonde and monthly averages, see Webster et al. (2016). For the Canberra area, radiosonde data were sourced from the Wagga Wagga meteorological station (Fig. 1), and for the Sydney area, radiosondes were averaged between Wagga Wagga and Sydney International Airport meteorological stations (Fig. 1).

From the interpolated meteorological and remotely sensed data, common surface energy balance (SEB) variables were derived, see Webster et al. (2016). This included the calculation of Leaf Area Index (LAI), Atmospheric Emissivity (ϵ_a), Surface Emissivity (ϵ_o), Surface Albedo (σ_s), Air Density (ρ), Net Radiation (R_N), Soil Heat Flux (G), and Roughness Length for Momentum (Z_{OM}). Timmermans et al. (2013) reported that SEBS λE was overestimated in tall canopies ($>1m$) when the roughness length for heat transport (Z_{OH}) was derived using the methods of Su (2002). So, we adopted a simplified definition of Z_{OH} (12), more applicable to heterogeneous landscapes (Garratt and Hicks, 1973) exhibited by the vegetation type and canopy height throughout our study areas (Fig. 1) (Keith, 2004).

$$Z_{OH} = \frac{Z_{OM}}{7} \tag{12}$$

Landsat 5 and 7 thermal data were sharpened using the TsHARP technique for Landsat imagery with a linear relationship to fractional vegetation cover. This configuration was

selected given its relative performance to other sharpening approaches outlined by (Agam et al., 2007). The processing steps used for thermal sharpening are provided in Appendix B of Webster et al. (2016). Reduced (60 m) aggregated pixel sizes were used to reflect the increased resolution of Landsat 7 thermal data in the Sydney study area.

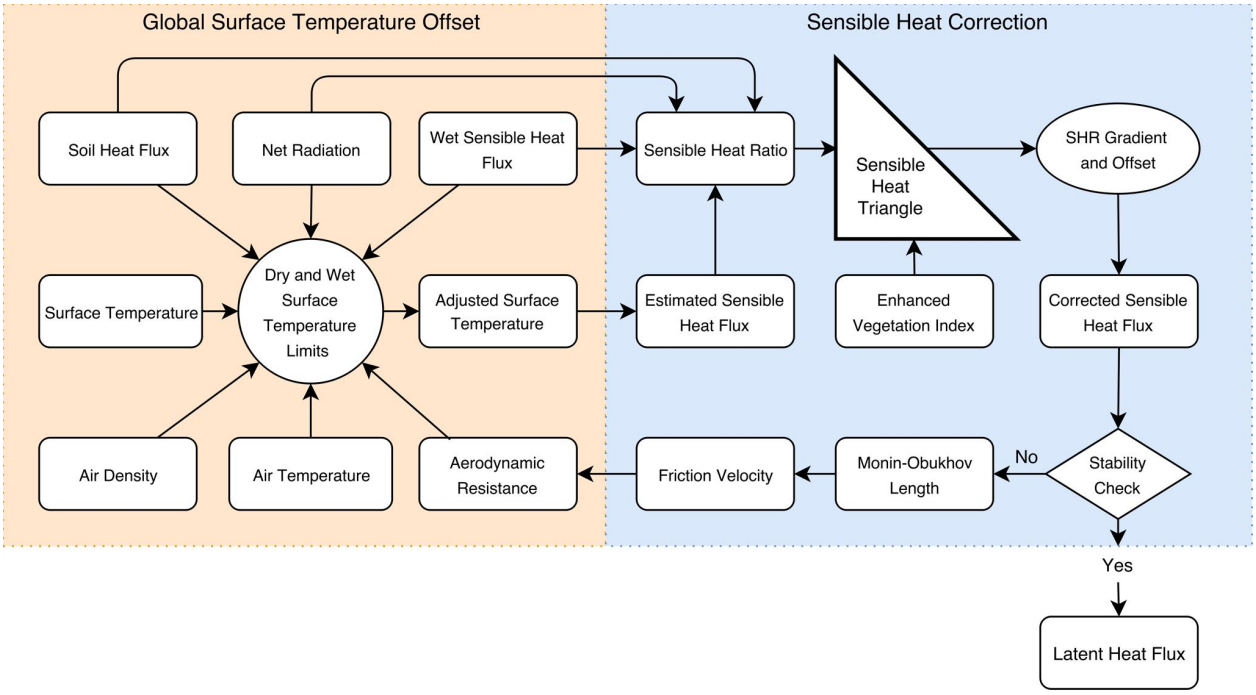

Figure 3: A flowchart depicting the two stage energy restraint incorporated into the Surface Energy Balance System. The first stage (orange shaded area) quantifies a global offset for surface temperature, while the second stage (blue shaded area) uses a domain-based image search routine to identify the limits of the Sensible Heat Ratio (SHR) to make a gradient and offset correction to sensible heat flux (H). The routine continues until the aerodynamic resistance and the gradient and offset correction parameters stabilise.

Before the SEBS-ER energy restraint of H, we identified and masked out inappropriate 30 x 30 m land units within each Landsat acquisition to ensure only clean vegetated land units were processed within the two stage energy restraint. They were masked if: EVI was less than -0.05 or greater than 1.2; terrain slope was greater than 30 degrees; the solar incidence ($cos\theta_i$) (Allen et al., 2007) was less than 0.3; the ratio of $H - H_{wet}$ to $AE - H_{wet}$ was less than -10 or greater than 10; or the land unit contained water, cloud or cloud shadows as defined by the Landsat classification mask (Masek et al., 2006).

The definition of SEBS-ER L, U_* and R_{AH} were consistent with previous SEBS definitions (Eq. 3, Eq. 2 and Eq. 1), and similarly, so were the SEBS-ER definitions for L_{wet} (8), R_{EW} (7) and H_{wet} (6). Our energy restraint executed in two stages to ensure H and λE were correctly partitioned with respect to AE within each consecutive iteration of R_{AH} (Fig. 3). This energy restraint is simply a corrective response to the errors and bias within the T_S

estimate (Allen et al., 2011b), the interpolative errors in the T_A and U_x estimates (Webster et al., 2016), and the limitations in the simplified representations for the roughness for heat and momentum transport within the SEBS algorithm (Timmermans et al., 2013). The first stage added a scene-wide offset to T_S (T_{Sadj}) to ensure the virtual difference between T_S and T_A was considerate of both the lower limit of H (H_{wet}), the upper limit of H (R_N-G), and mitigated any excessive underestimations or overestimations in R_{AH}. While this first stage was not designed to vastly improve the accuracy of the SEBS algorithm alone, it was critical to the successful resolution for the second stage of analysis, by ensuring that, on average, T_A did not exceed T_S. To determine the global surface temperature offset (Fig. 3), we used R_{AH} and ρ to estimate T_S at the wet limit (T_{Swet}) (13):

$$T_{Swet} = \frac{H_{wet}\, R_{AH}}{\rho\, C_p} + T_A \tag{13}$$

and T_S at the dry limit (T_{Sdry}) (14):

$$T_{Sdry} = \frac{(R_N - G) R_{AH}}{\rho\, C_p} + T_A. \tag{14}$$

Using T_{Swet} and T_{Sdry}, T_S was then adjusted (T_{Sadj}), by a global offset, to move the 50^{th} percentile of unmasked 30 x 30 m land units halfway between T_{Swet} and T_{Sdry} (15):

$$T_{Sadj} = T_S + 50^{th}\ percentile\ of\ \left(\frac{T_{Sdry} + T_{Swet}}{2} - T_S\right). \tag{15}$$

Given T_{Sadj}, we altered Eq. 4 to initially estimate H (H_E) (16):

$$H_E = \frac{\rho\, C_p\, (T_{Sadj} - T_A)}{R_{AH}} \tag{16}$$

and used it to define the sensible heat ratio (SHR) (17) to relate the difference between H_E and H_{wet} to the range of available evaporative energy ($R_N - G - H_{wet}$).

$$SHR = \frac{H_E - H_{wet}}{R_N - G - H_{wet}} \tag{17}$$

In the second stage of the energy restraint routine (Fig. 3), we collated the estimate of SHR against corresponding values of the enhanced vegetation index (EVI) (Masek et al., 2006). The resulting two-dimensional (2D) density distribution produced the sensible heat triangle (SHT) (Fig. 3 and Fig. 4), representative of conditions within the masked Landsat tile. EVI was used as an indicator of fractional vegetation cover as it provided improved delineation at the top of the sensible heat triangle, unlike $NDVI$ which is more prone to saturation (Huete et al., 2002). The image processing procedure for determining the

boundaries of the SHT are outlined in Appendix B. The lower SHR boundary (SHR_{MIN}) represented the cool and wet landscape limit of energy flux processes, represented by Eq. 5 (Fig. 4). Correspondingly, the upper SHR boundary (SHR_{MAX}) represented the hot and dry landscape limit of energy flux processes, where λE equals zero and H equals AE (Fig. 4).

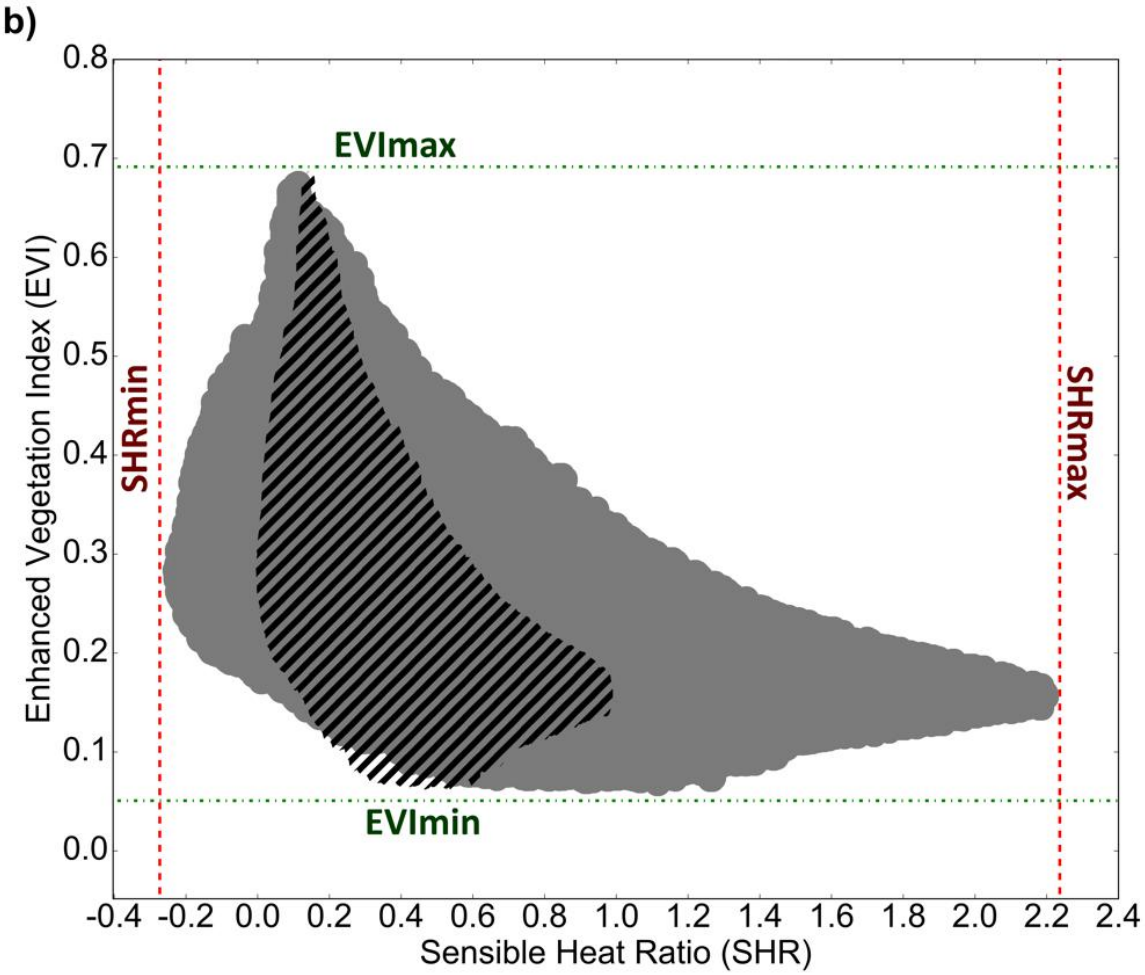

Figure 4: The constraint and adjustment of the SEBS-ER Sensible Heat Triangle (SHT), defined by SHR_{MAX} and SHR_{MIN} values and a gradient (A_{ER}) and intercept (B_{ER}) applied to adjust the input SHT distribution (shaded grey) to a new SHT with an SHR ranged between 0 and 1 (dark striped).

The automated image based estimates of SHR_{MIN} and SHR_{MAX} (Fig. 4) were then used to adjust H_E via linear gradient (A_{ER}) and intercept (B_{ER}) coefficients (18) to obtain a corrected sensible heat flux (H_C), appropriately constrained with respect to AE (Fig. 4).

$$\frac{H_C - H_{wet}}{R_N - G - H_{wet}} = A_{ER}\left(\frac{H_E - H_{wet}}{R_N - G - H_{wet}}\right) + B_{ER} \tag{18}$$

To determine A_{ER} and B_{ER} and constrain the range of SHR between 0 and 1 (Fig. 4), the

hot and dry limit, SHR_{MAX}, was used (19):

$$\frac{H_E - H_{wet}}{R_N - G - H_{wet}} = SHR_{MAX} \rightarrow \frac{H_C - H_{wet}}{R_N - G - H_{wet}} = 1.0 \tag{19}$$

with the max evaporative limit, SHR_{MIN} (20):

$$\frac{H_E - H_{wet}}{R_N - G - H_{wet}} = SHR_{MIN} \rightarrow \frac{H_C - H_{wet}}{R_N - G - H_{wet}} = 0.0 \tag{20}$$

to solve a solution for A_{ER} (21):

$$A_{ER} = \frac{1.0}{SHR_{MAX} - SHR_{MIN}} \tag{21}$$

and B_{ER} (22):

$$B_{ER} = -\frac{SHR_{MIN}}{SHR_{MAX} - SHR_{MIN}}. \tag{22}$$

A_{ER} and B_{ER} were then used with Eq. 18 to derive H_C explicitly (23):

$$H_C = A_{ER}(H_E - H_{wet}) + B_{ER}(R_N - G - H_{wet}) + H_{wet}. \tag{23}$$

This geospatial processing and image analysis sequence (3, 2, 1, 13, 14, 15, 16, 8, 7, 6, 18, 21, 22 and 23) was repeated with MO corrections until consecutive estimates of A_{ER} and B_{ER} differed by less than 1.5%. At this point λE was solved as the residual of the energy balance (24):

$$\lambda E = R_N - G - H_C. \tag{24}$$

4.2. Sensitivity of SEBS and SEBS-ER to Input Error

The SEBS and SEBS-ER sensitivity analysis were conducted only in the Canberra study area, as impacts from land use change and disturbance events within the Sydney area would have likely complicated the results. We tested the sensitivity against six input variables, used in the calculation of SEB and SEBS-ER H and λE. The inputs consisted of two key remotely sensed variables (T_S and Z_{om}) (Petropoulos et al., 2009b) and four key meteorological variables (T_A, U_x, P_{vap}, and δ) (Elhag, 2016; Webster et al., 2016). For the analysis, T_S and T_A 30 x 30 m land units were randomly perturbed by 2 ^oC (Yang and Shang, 2013), while U_x, P_{vap}, and δ land units were randomly perturbed by 20% (Yang and Shang, 2013). Following the analysis by Timmermans et al. (2013), Z_{om} land units were randomly perturbed by 50%. For each acquisition date, separate estimations of λE were obtained from SEBS and SEBS-ER for the variation of each sensitivity input, while the remaining five variables were left unperturbed. The sensitivity of SEBS and SEBS-ER λE were then derived for each

input variable ($\Delta\lambda E_{VAR}$) (25) (Yang and Shang, 2013), collated across the four acquisition dates:

$$\Delta\lambda E_{VAR} = \frac{\lambda E_{pert} - \lambda E_{init}}{100(VAR_{pert} - VAR_{init})/VAR_{init}}, \quad (25)$$

where λE_{pert} was the λE from the perturbed input (VAR_{pert}) and λE_{init} was the λE from the unperturbed input (VAR_{init}). Linear regressions of the resultant distributions were then used to compare the relative sensitivity of SEBS and SEBS-ER to variation in each of the six input variables. Additionally, average spatially explicit grids of the absolute sensitivity of λE per percent change in each input variable were plotted for SEBS and SEBS-ER.

4.3. Validation and Performance of SEBS and SEBS-ER

Validation was conducted within the Canberra study area across the nine acquisition dates (Fig. 2a). The two flux towers, in contrasting land types, were used to compare the relative accuracy of the existing SEBS algorithm to the new SEBS-ER technique. All input data were consistent between the two algorithms, producing common estimates of Z_{OM}, Z_{OH}, ρ, σ_s, R_N, and G. λE was used rather than ET_a, as the basis for comparison to the two flux towers, to remove the uncertainty and errors associated with the temporal scaling of instantaneous fluxes to daily ET_a estimates (Van Niel et al., 2012, 2011). SEBS and SEBS-ER λE estimates were compared to HTEM and S-SEBI data obtained from Webster et al. (2016). At the 70 m high Tumbarumba flux tower (Fig. 1), a 750 m radial footprint (see van Gorsel et al., 2013) was used to sample λE from S-SEBI, HTEM, SEBS, and SEBS-ER outputs on each of the nine acquisition dates in the Canberra study area (Fig. 2a). At the 2.5 m high Nimmo High Plains flux tower (Fig. 1), a 30 m radial footprint was used for sampling given the comparative height between the two towers and the lower canopy height (Scarth, 2014). This tower only recorded λE data on the 9 Mar 2007, 12 May 2007, and 1 Sep 2007 acquisition dates. For each flux tower and acquisition date compared, the mean and plus or minus two standard deviations from the collection of 30 x 30 m land unit samples were plotted against flux tower λE for S-SEBI, HTEM, SEBS, and SEBS-ER.

4.4. Temporal Stability of SEBS and SEBS-ER

Fifty-two acquisitions of Landsat 5 and 7 data from the Sydney study area were combined with meteorological and land use data to produce daytime estimates of ET_a for both SEBS and SEBS-ER. Given the outcomes from Van Niel et al. (2011) and Van Niel et al. (2012), the temporal scaling of λE, from Eq. 24, was restricted to a daytime only estimate of ET_a

for SEBS and SEBS-ER, using the daily/daytime quantification of solar exposure (δ) and the assumption that Λ was constant over daytime hours (26):

$$ET_a = \Lambda \frac{\delta\,(1-\sigma_s)}{\lambda\,\rho_w}, \tag{26}$$

where ρ_w was the density of water (1.000 kg m^{-3}).

We compared the 52 SEBS and SEBS-ER daily ET_a maps in the Sydney study area (Fig. 1) against a daily 250 m ET_a dataset in the absence of field based ET_a measures or other forms of validation data. While the comparison between two ET_a algorithms was not ideal in terms of assessing absolute accuracy, such as that from a localised flux tower, it did enable a spatially explicit scene-wide comparison to be drawn among all land units across the landscape. The 250 m daily ET_a dataset was derived from a realisation of the PT-JPL algorithm (Fisher et al., 2008) executed using: the MOD13Q1 NDVI product (USGS, 2009); the SRTM v3 1 arc second elevation product (Gallant et al., 2011); and BOM T_M, T_X, P_{vap}, P_{sat}, and δ observation data, the same as that used for SEBS and SEBS-ER ET_a estimates. To allow direct comparison, 30 m SEBS and SEBS-ER ET_a data were first resampled to 250 m by aggregation.

The PT-JPL algorithm was adapted from the data model provided by Fisher et al. (2008) (josh.yosh.org/datamodels.htm) for use with spatial grids of NDVI and meteorological data. PT-JPL is a process driven model (Fisher et al., 2008), well suited to derive temporally continuous and accurate estimations of ET_a (Chen et al., 2014), using coarse scale data such as MODIS (Yao et al., 2013). It relies on comparatively little input data and does not require thermal infrared data, unlike SEBS or SEBS-ER, making it more temporally stable than SEBS and better suited to continuous daily realisations of ET_a data (Yao et al., 2013). Given this, the validation using PT-JPL ET_a data was directed and limited towards assessing the temporal stability of SEBS-ER, compared to SEBS within the Sydney study area (Fig 1).

To achieve a comprehensive comparison between SEBS/SEBS-ER and PT-JPL data, we undertook three aspects of analysis. First, we determined the spatially explicit ET_a RMSE between SEBS and SEBS-ER to PT-JPL data across all 52 acquisition dates, then we produced density distribution plots comparing ET_a between SEBS and SEBS-ER to PT-JPL, and finally we subset the mean absolute error between SEBS and SEBS-ER to PT-JPL by season. The final form of validation data we used were pan evaporation records for two BOM stations within the Sydney study area (Fig. 1). Pan evaporation records can not be used as a direct form of validation for ET_a data (McMahon et al., 2013) but they do

signify the upper limit of expected ET_a values and they were therefore used only to assess the overestimation of SEBS and SEBS-ER ET_a estimates.

5. Results

5.1. Integration of a SEBS Energy Restraint

SEBS-ER successfully estimated SEB energy fluxes for nine Landsat acquisitions in the Canberra study area (Fig. 2a) and 52 Landsat acquisitions in the Sydney study area (Fig. 2b). There was variation in stage one T_S offset and the stage two SHR gradient (A_{ER}) and intercept (B_{ER}) correction coefficients (Table 1), reflected in the initial SHR-EVI sensible heat triangles for the Canberra study area among dates (Fig. 5). Stage one T_S offsets varied between -4.5 K (5 Feb 2007) and 10.8 K (26 Feb 2009), while stage two coefficients showed greater stability with a range of 0.109 (1 Sep 2007) - 0.448 (25 Jan 2009) for A_{ER} and 0.072 (25 Jan 2009) - 0.328 (5 Feb 2007) for B_{ER} (Table 1). Across all Canberra dates, the average T_S offset was 3.19 K with high variability while A_{ER} and B_{ER} corrections were comparatively stable, around 0.242 and 0.201 respectively (Table 1).

Table 1: Summary of the SEBS-ER calibration parameters for the final Monin Obukhov (MO) iteration used for all nine acquisition dates in the Canberra study area (Fig. 2a). The T_S offset was the global shift that centred the distribution between the theoretical wet and dry T_S limits, while the SHR (Sensible Heat Ratio) gradient and intercept coefficients constrained the range of SHR, between the limits of available evaporative energy, ranged between zero and one. The mean and standard deviation (SD) were calculated from all Canberra acquisition dates (Fig. 2a).

Date	T_S offset (K)	SHR Gradient	SHR Intercept
17 Nov 2006	2.48	0.340	0.224
5 Feb 2007	-4.51	0.142	0.328
9 Mar 2007	3.98	0.352	0.217
26 Apr 2007	3.78	0.201	0.221
12 May 2007	3.61	0.119	0.298
1 Sep 2007	4.64	0.109	0.091
8 Dec 2008	0.64	0.181	0.227
25 Jan 2009	7.89	0.290	0.072
26 Feb 2009	10.77	0.448	0.134
Mean (SD)	3.70 (4.04)	0.242 (0.113)	0.201 (0.082)

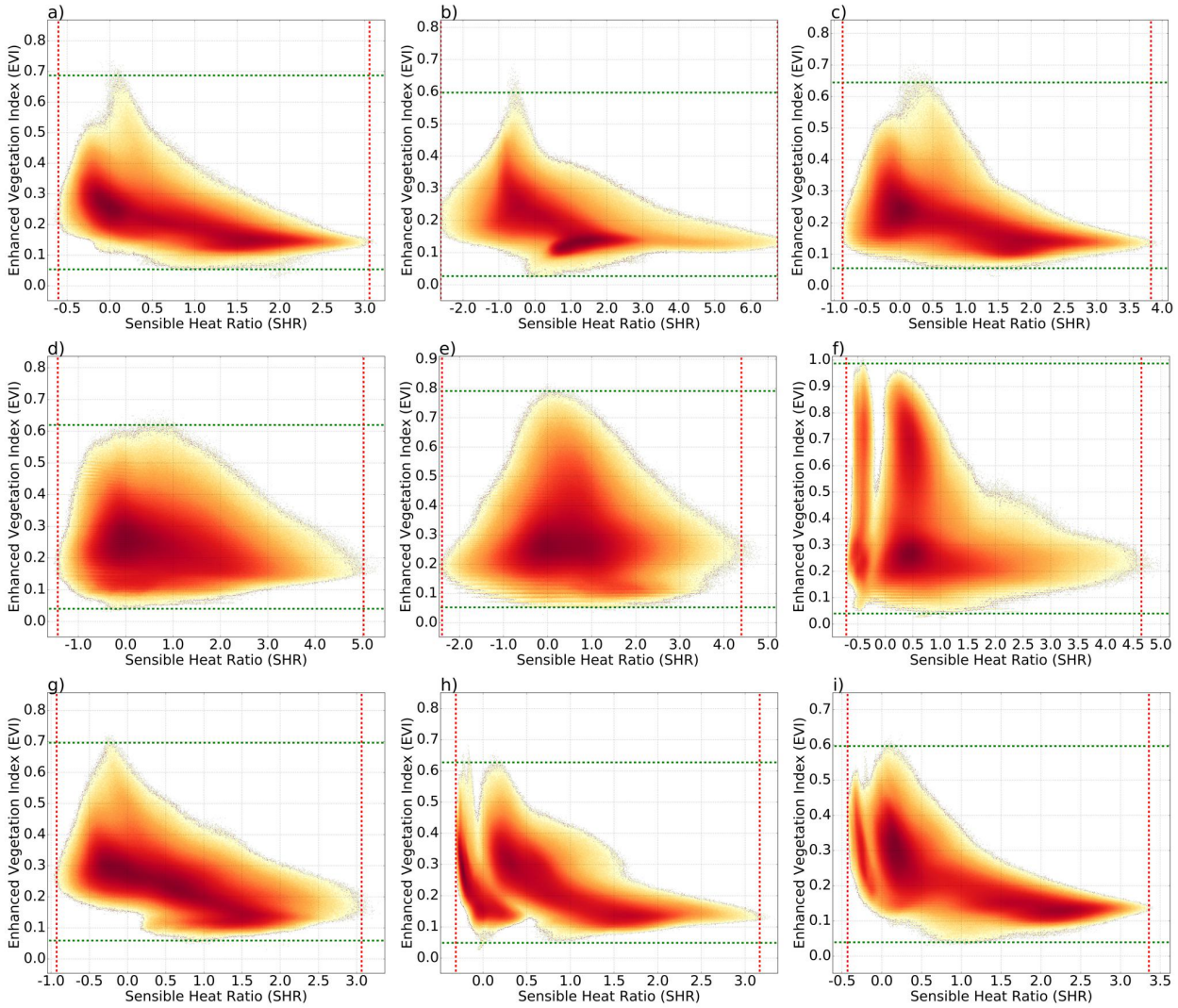

Figure 5: Sensible Heat Triangles (SHT) showing the density distribution of the Sensible Heat Ratio (SHR) to the Enhanced Vegetation Index (Vegetation Fraction) for a) 17 Nov 2006, b) 5 Feb 2007, c) 9 Mar 2007, d) 26 Apr 2007, e) 12 May 2007, f) 1 Sep 2007, g) 8 Dec 2008, h) 25 Jan 2009 and j) 26 Feb 2009, where darker colours indicated higher densities. The horizontal dashed lines were the derived upper and lower limits of vegetation cover, while the vertical dashed lines represented the derived upper and lower limits of evaporative energy.

All SHT plots had a consistent shape and form across the nine Canberra acquisition dates, with a distinctive vertex denoting the boundary for SHR_{MAX} (right-hand side) and long flat edge denoting the boundary for SHR_{MIN} (left-hand side) (Fig. 5). The SHT plots for 1 Sep 2007, 25 Jan 2009, and 26 Feb 2009 had two separate and distinct distribution clusters near the left edge (Fig. 5), the cool and wet SHR boundary. These patterns were spatially coincident with low wind speeds, $<1\ m\ s^{-1}$, that led to comparatively large R_{AH} values near relevant ground stations for each date. Comparatively high stage one T_S offsets (7.89 K and 10.77 K respectively) were also recorded for these dates (Table 1). Also,

for the larger 1 Sep 2007 SHT disconnection, the effect was spatially coincident with a comparatively small R_{AH} and a comparatively large T_S to T_A difference surrounding the snow covered alpine areas, common for early September in the Australian Alps. The 5 Feb 2007 SHT plot exhibited a distinct density cluster midway along the lower edge of the SHT (Fig. 5), spatially coincident with stable SHR and R_{AH} values in the agricultural and grazing areas in the north-west corner of the Canberra study area (Fig. 1). The 5 Feb 2007 SHT plot also had the only negative T_S offset and the highest B_{ER} coefficient across the nine Canberra acquisition dates (Fig. 2a and Table 1).

5.2. Sensitivity of SEBS and SEBS-ER to Input Error

Compared to SEBS, SEBS-ER showed less sensitivity to perturbation for each of the six input variables analysed (T_S, T_A, δ, Z_{OM}, U_x, and P_{vap}) (Fig. 6). Overall, SEBS and SEBS-ER were more sensitive to the variation of T_S, T_A, and δ than Z_{OM}, U_x, and P_{vap} (Fig. 6 and Fig. 7). However, SEBS-ER showed residual variation in λE when variation in the input variable was zero (Fig. 6), while apart from T_S, SEBS indicated no residual variation in λE across input variables (Fig. 6). Individually, SEBS-ER had substantially lower sensitivity in λE values for T_S, moving from -5.37 $W\,m^{-2}$ to -1.67 $W\,m^{-2}$ per percent change in T_S (Fig. 6). Similarly, SEBS-ER was substantially less sensitive than SEBS to changes in T_A, moving from 4.30 $W\,m^{-2}$ to 1.59 $W\,m^{-2}$ per percent change in T_A (Fig. 6). The sensitivity distribution pattern for T_S and T_A varied slightly between acquisition dates, indicated by comparatively lower R^2 values (Fig. 6). The sensitivity of SEBS to δ was similar to that of T_S, with a a change of 5.67 $W\,m^{-2}$ per percent change in δ. The coherence, among acquisition dates, in the response to δ perturbation was strong with comparatively high R^2 values (Fig. 6). The sensitivity of SEBS-ER to δ was about two thirds that of SEBS, at 3.81 $W\,m^{-2}$ per percent change in δ.

While overall the λE sensitivity of SEBS and SEBS-ER were lower for Z_{OM}, U_x and P_{vap}, the comparative relationship between SEBS and SEBS-ER was similar to T_S, T_A and δ. For both SEBS and SEBS-ER, the variation in λE sensitivity among acquisition dates and 30 x 30 m land units were the largest for U_x and Z_{OM}, highlighted by lowest R^2 statistics (Fig. 6). The sensitivity response distributions were also similar for U_x and Z_{OM} with SEBS-ER showing asymmetrically greater variation in sensitivity for a negative shift in U_x and Z_{OM} input values. For both U_x and Z_{OM}, the reduction in sensitivity to perturbations was just above 50% for SEBS-ER, compared to SEBS (Fig. 6). SEBS and SEBS-ER were least sensitive to perturbations in P_{vap}, per percent change, with λE changes of just 0.372 $W\,m^{-2}$

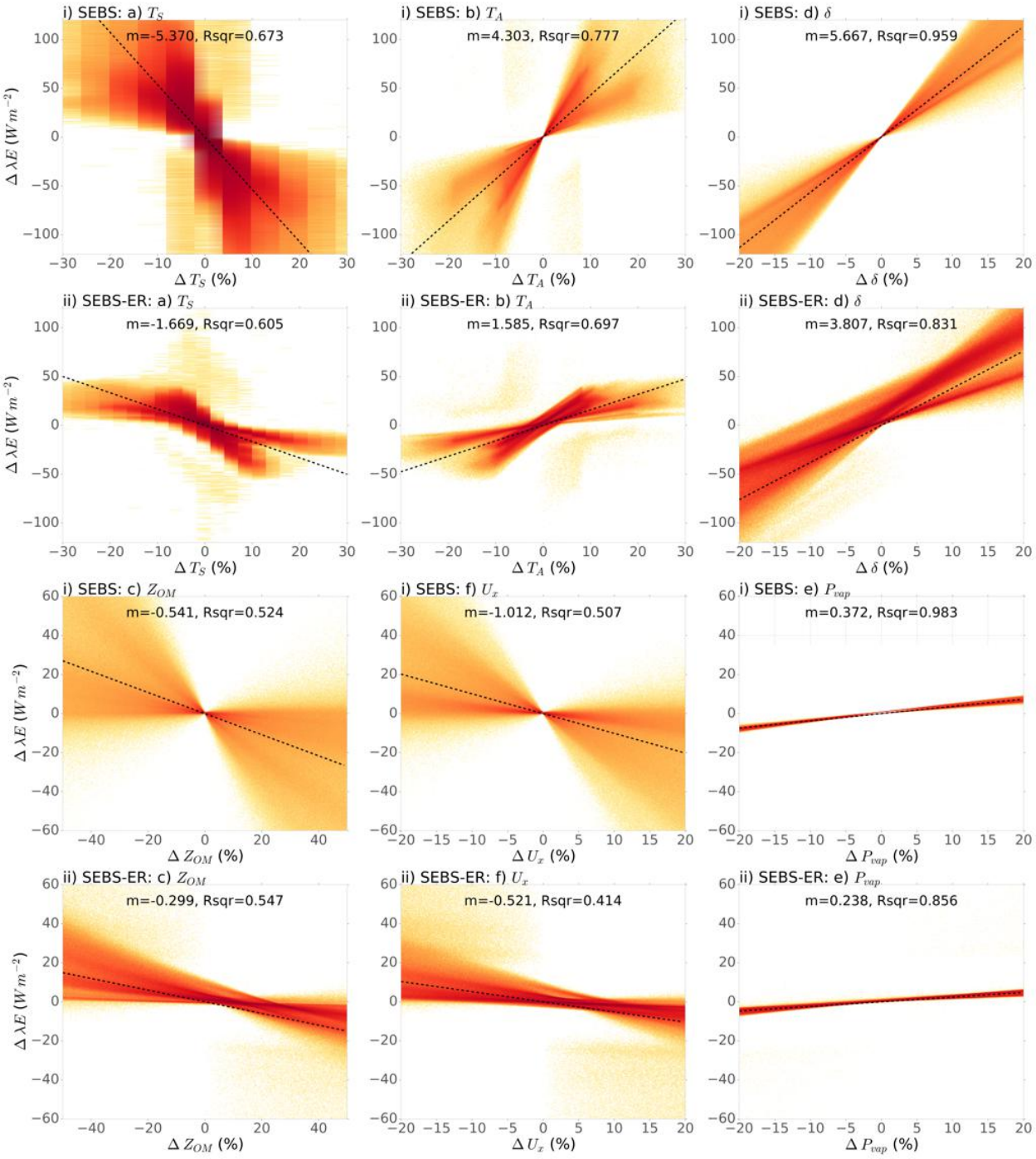

Figure 6: Temporally averaged comparisons of λE input sensitivity for i) SEBS and ii) SEBS-ER surface energy balance algorithms after perturbing different input variables: a) surface temperature (T_S); b) air temperature (T_A); c) daily solar exposure (δ); d) surface roughness (Z_{OM}); e) wind speed (U_x); and f) vapour pressure (P_{vap}), where darker shading represented higher densities. Linear regressions between the change in λE to the % change of each input parameter were represented by dashed black lines, with the gradient coefficient (m) and R^2 statistic displayed at the top of each density plot.

for SEBS and 0.238 $W\ m^{-2}$ for SEBS-ER. Of the six input variables, P_{vap} sensitivity was also the most coherent for SEBS and SEBS-ER, among acquisition dates and 30 x 30 m land units.

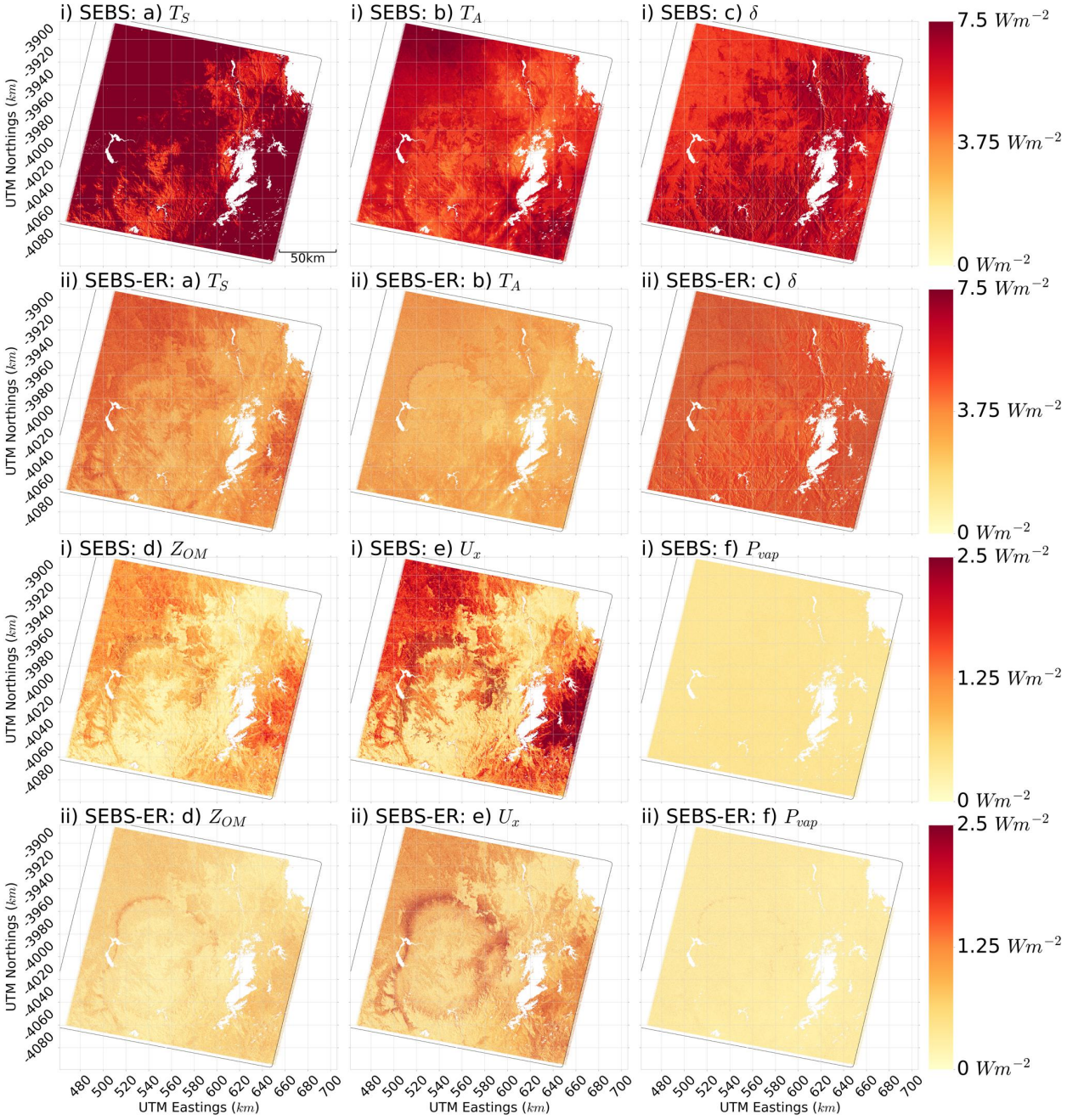

Figure 7: Temporally averaged spatial grids of λE sensitivity from perturbation in (i) SEBS and (ii) SEBS-ER input variables in the Canberra study area (black polygon). Grids show the relative spatial change in λE related to a 1% change in (a) surface temperature (T_S, $^{\circ}C$), (b) air temperature (T_A, $^{\circ}C$), (c) solar exposure (δ, $MJ\,day^{-1}$), (d) surface roughness for momentum (Z_{OM}, m), (e) wind speed (U_x, $m\,s{-}1$), and (f) vapour pressure (P_{vap}, kPa). Note the scale change between T_S, T_A and δ (0 - 7.5 $W\,m^{-2}$) and Z_{OM}, U_x and P_{vap} (0 - 2.5 $W\,m^{-2}$). UTM Eastings and Northings were for Zone 55 North.

Average spatial grids of λE sensitivity (per percent input change) to perturbations in T_S, T_A, δ, Z_{OM}, U_x, and P_{vap} (Fig. 7) reflected the sensitivity distributions (Fig. 6), with consistently lower sensitivities by SEBS-ER, compared to SEBS. The spatial grids also reinforced the difference in magnitude between T_S, T_A, and δ inputs, compared to Z_{OM},

U_x, and P_{vap} inputs (Fig. 7). For SEBS, the sensitivity to T_S was smaller in forested areas than agricultural or grazing areas (Fig. 1 and Fig. 7). This pattern was substantially less pronounced in the SEBS-ER T_S sensitivity grid, featuring a more spatially uniform sensitivity response (Fig. 7). Similarly, the T_A sensitivity response was greater in the north-west and south-east corners of the study area, while the SEBS-ER T_A sensitivity grid was spatially uniform (Fig. 7). The SEBS δ sensitivity grid exhibited a high response in forested areas compared to agricultural, grassland, or grazing land types. Like T_S and T_A, the δ, Z_{OM}, U_x, and P_{vap} sensitivity response grids for SEBS-ER were spatially uniform and smaller in magnitude than SEBS (Fig. 7). Also, like the sensitivity distribution plots in Figure 6, the SEBS Z_{OM} and U_x sensitivity spatial grids indicated similar spatial patterning, with increased sensitivity along the low vegetation height land types along the eastern boundary and in the north-west corner of the study area (Fig. 1 and Fig. 7). Finally, compared to the other input variables, P_{vap} exhibited a negligible and spatially uniform sensitivity grid for SEBS, also indistinguishable from that of SEBS-ER (Fig. 7).

5.3. Validation and Performance of SEBS and SEBS-ER

Using all available λE measurements from the two eddy covariance flux towers (Fig. 1), we compared the accuracy of the SEBS and SEBS-ER surface energy balance algorithms (Fig. 8, Fig. 9, Table 2, and Table 3). Among the four algorithms validated using the Tumbarumba and Nimmo High Plains flux towers, SEBS-ER produced the smallest RMSE and the highest R^2 (Table 2) at each tower, and the smallest RMSE and highest R^2 overall (Table 3). Using an F test, SEBS-ER also showed a significant increase in performance (<0.05) from SEBS when calculated from all 12 flux tower comparisons. At the forested Tumbarumba flux tower, both SEBS and SEBS-ER varied in their estimates of λE among dates, both above and below the observed flux tower values (Fig. 8), however, SEBS-ER was substantially more accurate, with a RMSE of just 62.3 $W\ m^{-2}$ compared to an RMSE of 110.8 $W\ m^{-2}$ for SEBS (Table 2). The HTEM algorithm produced an RMSE slightly greater than SEBS (133.0 $W\ m^{-2}$) and the S-SEBI algorithm produced the largest RMSE of λE (148.2 $W\ m^{-2}$) (Table 2). Comparing the nine acquisition dates, SEBS-ER produced the closest λE estimate for seven (5 Feb 2007, 9 Mar 2007, 26 Apr 2007, 12 May 2007, 8 Dec 2008, 25 Jan 2009 and 26 Feb 2009), with SEBS producing the nearest λE estimate on 17 Nov 2006 and 1 Sep 2007 (Fig. 8). On four dates (9 Mar 2007, 26 Apr 2007, 12 May 2007 and 8 Dec 2008), SEBS-ER produced very close λE estimates that were less than 30 $W\ m^{-2}$ from Tumbarumba flux tower observations, producing an RMSE of just 13.4 $W\ m^{-2}$ across

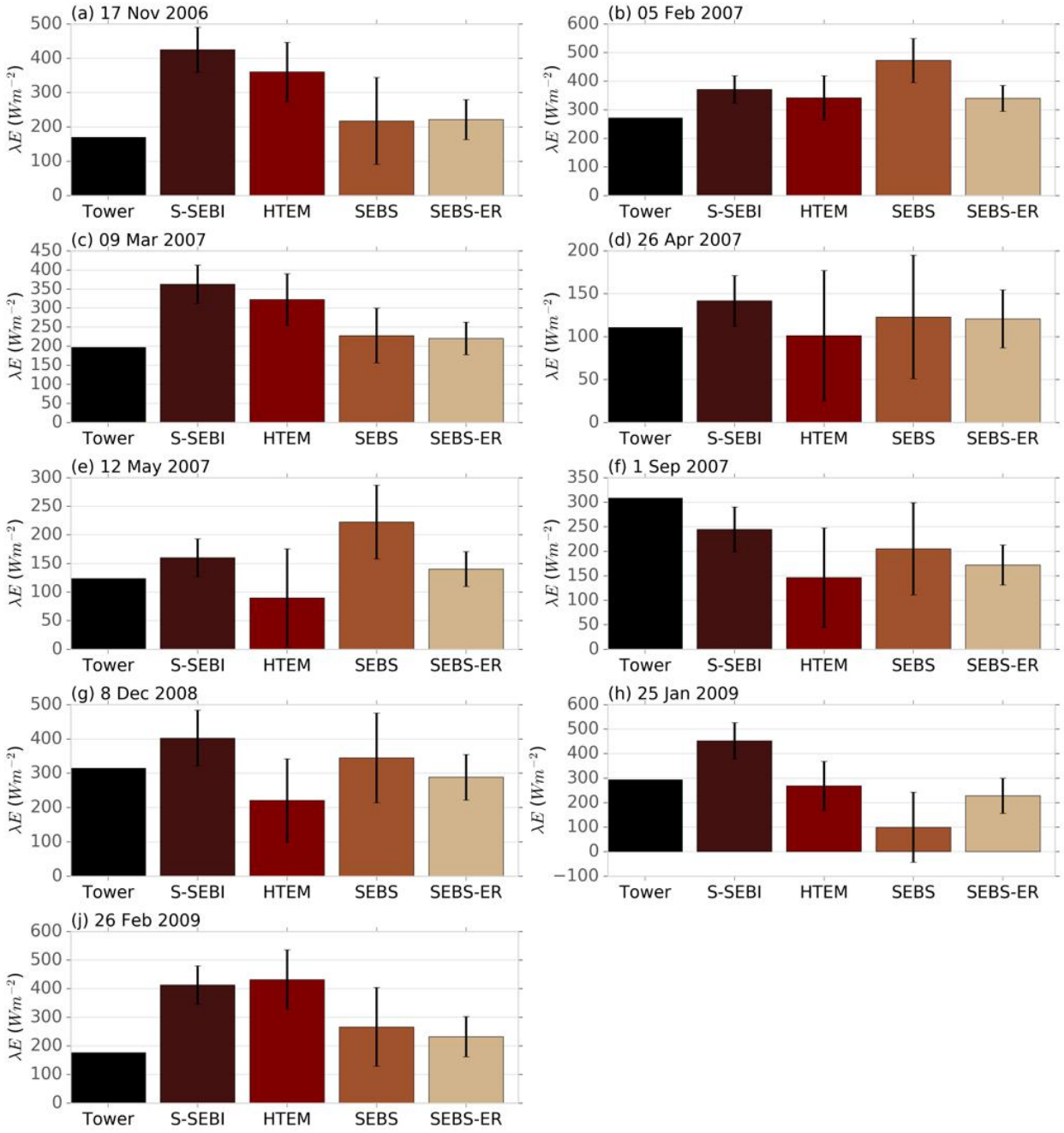

Figure 8: 750 m radial samples of λE ($W\ m^{-2}$) (± 2 SD) from S-SEBI and HTEM (Webster et al., 2016) and SEBS and SEBS-ER, compared to λE observed at the Tumbarumba flux tower (black) (Fig. 1) for the nine acquisition dates: (a) 17 Nov 2006; (b) 5 Feb 2007; (c) 9 Mar 2007; (d) 26 Apr 2007; (e) 12 May 2007; (f) 1 Sep 2007; (g) 8 Dec 2008; (h) 25 Jan 2009; and (j) 26 Feb 2009.

these four dates. For all three acquisition dates available for comparison at the Nimmo High Plains flux tower, SEBS-ER λE were closer to the flux tower estimate than SEBS (Fig. 9), with RMSE's of 32.2 $W\ m^{-2}$ and 80.6 $W\ m^{-2}$ respectively (Table 2). In the sub-alpine grassland land cover, the RMSE's for S-SEBI (50.3 $W\ m^{-2}$) and HTEM (41.8 $W\ m^{-2}$) were lower than SEBS but larger than SEBS-ER (Table 2). All four algorithms overestimated

λE on 1 Sep 2007 (Fig. 9), however, the RMSE for SEBS-ER was just 3.4 $W\ m^{-2}$ for the combined 9 Mar 2007 and 12 May 2007 dates.

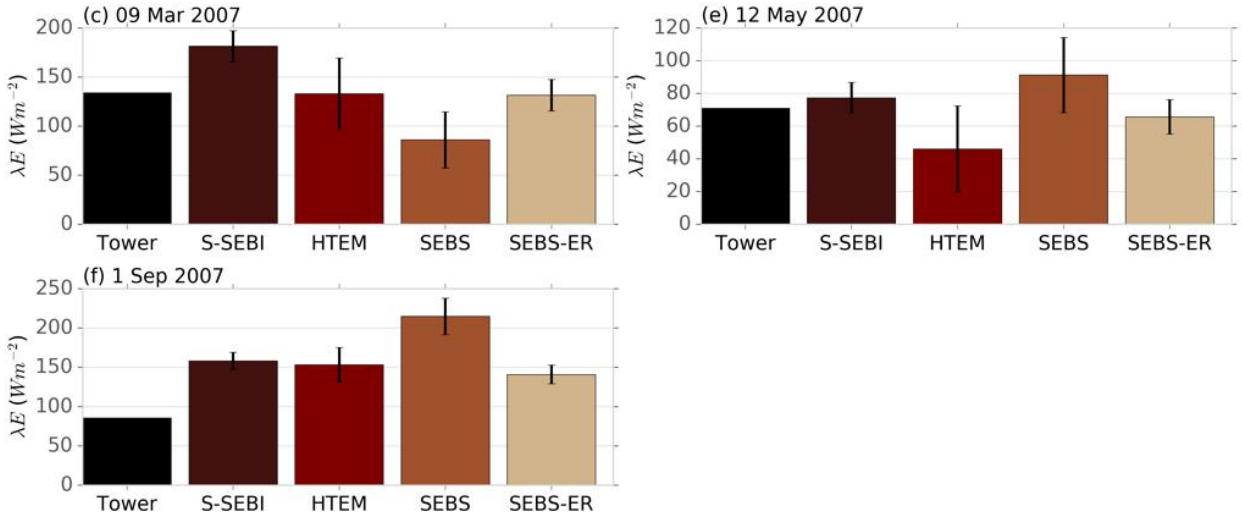

Figure 9: 30 m radial samples of λE ($W\ m^{-2}$) ($\pm$2 SD) from S-SEBI and HTEM (Webster et al., 2016) and SEBS and SEBS-ER, compared to λE observed at the Nimmo High Plains flux tower (black) (Fig. 1) for three acquisition dates: (c) 9 Mar 2007; (e) 12 May 2007; and (f) 1 Sep 2007.

Table 2: λE RMSE ($W\ m^{-2}$) and R^2 of S-SEBI, HTEM, SEBS, and SEBS-ER surface energy balance algorithms for all acquisition dates compared to the a) Tumbarumba and b) Nimmo High Plains flux towers.

Tower	Metric	S-SEBI	HTEM	SEBS	SEBS-ER
a)	RMSE	148.2 $W\ m^{-2}$	133.0 $W\ m^{-2}$	110.8 $W\ m^{-2}$	62.3 $W\ m^{-2}$
	R^2	0.819	0.772	0.824	0.879
b)	RMSE	50.3 $W\ m^{-2}$	41.8 $W\ m^{-2}$	80.6 $W\ m^{-2}$	32.2 $W\ m^{-2}$
	R^2	0.881	0.879	0.685	0.939

Table 3: Overall λE RMSE ($W\ m^{-2}$), R^2, and F statistic between SEBS and SEBS-ER for all 12 flux tower comparisons.

Algorithm	RMSE	R^2	SEBS→SEBS-ER F stat (P value)
SEBS	104.1 $W\ m^{-2}$	0.812	3.42 (0.02651)
SEBS-ER	56.3 $W\ m^{-2}$	0.925	

5.4. Temporal Stability of SEBS and SEBS-ER

Averaged over the 52 acquisition dates and compared to SEBS ET_a outputs, SEBS-ER exhibited substantially lower RMSE both spatially and seasonally, compared to the daily

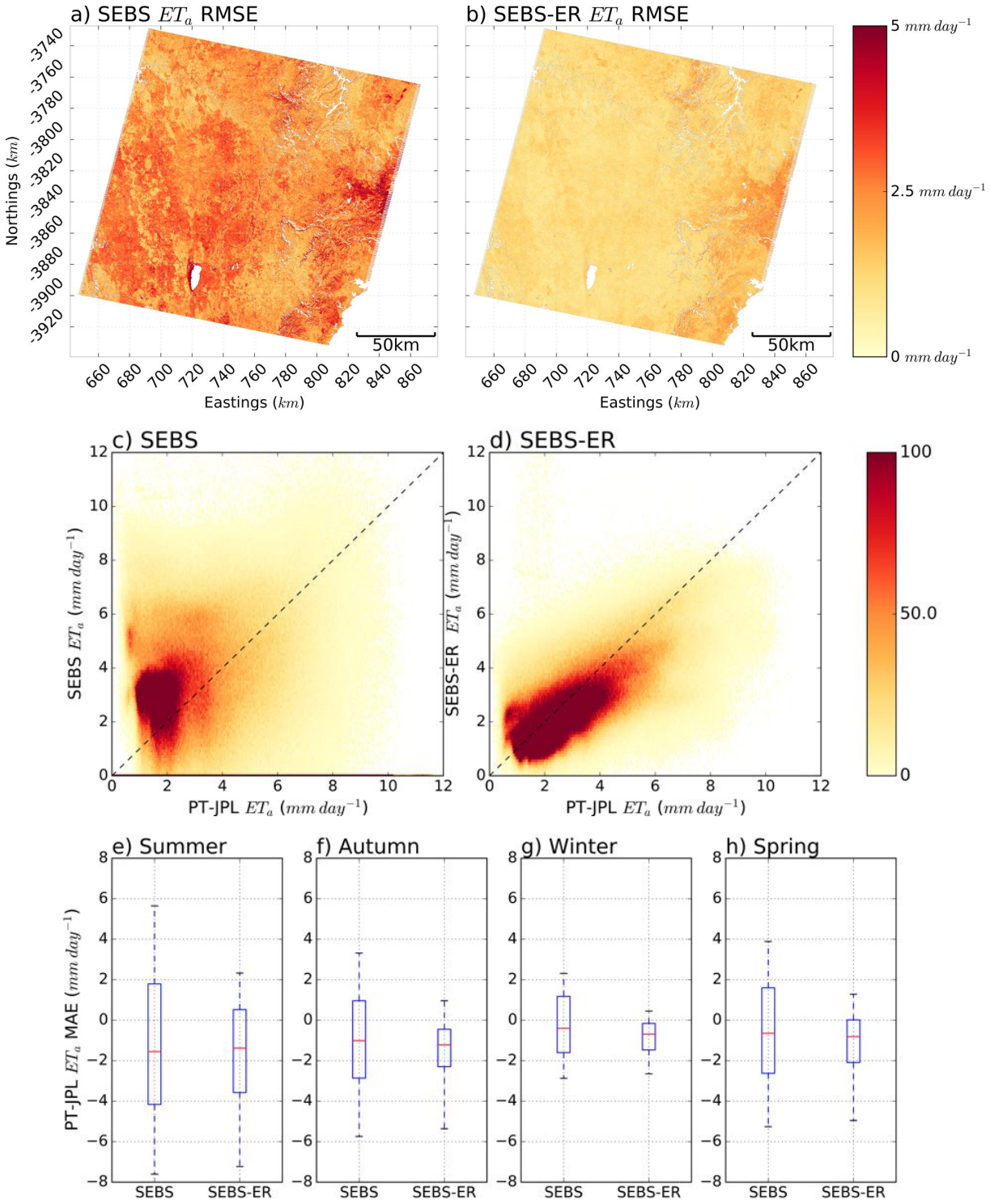

Figure 10: Multifaceted comparison of SEBS and SEBS-ER ET_a to daily PT-JPL ET_a data, showing the temporal average root mean square error (RMSE) spatially ($mm\,day^{-1}$) of (a) SEBS and (b) SEBS-ER and the comparisons of density distributions between PT-JPL ET_a to (c) SEBS ET_a and (d) SEBS-ER ET_a. Seasonal differences in SEBS and SEBS-ER ET_a, compared to PT-JPL ET_a were captured in estimates of mean absolute error (MAE), ($mm\,day^{-1}$) for acquisitions in (e) summer, (f) autumn, (g) winter, and (h) spring.

archive of PT-JPL data (Fig. 10). Additionally, SEBS-ER had greater coherence over the range of PT-JPL ET_a data, with SEBS generally overestimating ET_a compared to PT-JPL ET_a data (Fig. 10). In the RMSE spatial grids, SEBS ET_a error was greater over non-forested areas of the Sydney study area, with SEBS-ER exhibiting a spatially uniform distribution of error (Fig. 10). Seasonally, compared to SEBS and referenced to PT-JPL ET_a data, SEBS-ER had less variation in mean absolute error (MAE) in summer and substantially reduced variation in MAE in autumn, winter, and spring (Fig. 10). Across the seasons, as indicated by MAE, SEBS-ER generally underestimated PT-JPL ET_a estimates, while SEBS overestimated in winter, underestimated in summer and spring, and was on parity in autumn (Fig. 10).

Also in the Sydney study area (Fig. 1), SEBS-ER reduced ET_a overestimation exhibited by SEBS when compared to pan evaporation data (Fig. 11) from two meteorological ground stations across cloud free acquisition dates. However, both SEBS and SEBS-ER were prone to overestimating ET_a when compared to smaller ET_o pan evaporation observations. Between the two pan evaporation stations, compared values and errors were evenly spread, with no discernible difference in input (ET_o) or estimated (ET_a) magnitudes (Fig. 11).

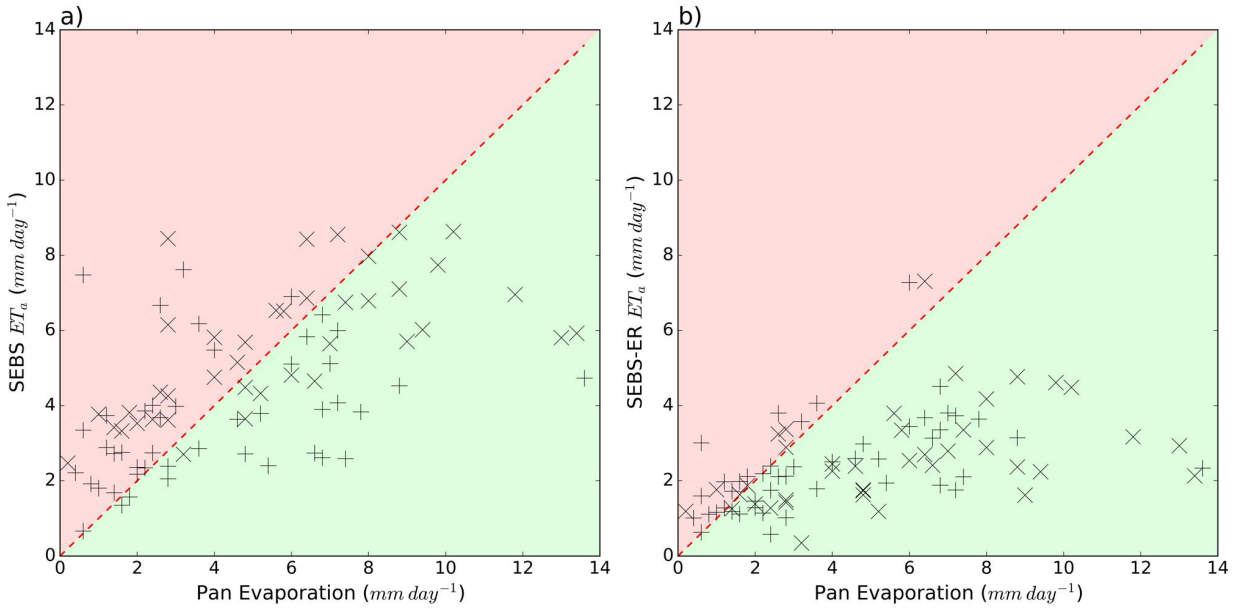

Figure 11: Daily pan evaporation data ($mm\,day^{-1}$) from stations (x) 070014 and (+) 070263 in the Sydney study area (Fig. 1) over a ten year period (Fig. 2b) compared to actual evapotranspiration (ET_a, $mm\,day^{-1}$) from (a) SEBS and (b) SEBS-ER. The red shaded area indicates unrealistic estimates of SEBS and SEBS-ER ET_a and the green shaded area indicates valid SEBS and SEBS-ER ET_a estimates.

6. Discussion

The addition of an energy restraint to SEBS (Su, 2002) within the MoninObukhov iterative correction to H was largely successful. SEBS-ER effectively resolved energy fluxes from nine Landsat acquisitions in the Canberra study area (Fig. 2a) and energy fluxes from 52 Landsat acquisitions from the Sydney study area (Fig. 2b). Compared to SEBS, SEBS-ER improved resilience to perturbation from six input variables (Fig. 6 and Fig. 7), produced significantly greater accuracy at two flux tower locations (Table 2, and Table 3), and provided greater temporal stability against pan evaporation data (Fig. 11) and a daily PT-JPL ET_a dataset (Fig. 10).

6.1. Development of the SEBS energy restraint

T_S-VI SEB techniques have developed a considerable amount in recent years (Gampe et al., 2016; Knipper et al., 2016; Lian and Huang, 2016; Long and Singh, 2012; Long et al., 2012; Yang and Shang, 2013), but our SEBS-ER approach is the first implementation of a direct flux based energy restraint, within a domain based triangular framework. Unlike other triangular (Gampe et al., 2016; Knipper et al., 2016) or trapezoidal (Long and Singh, 2012) techniques, our energy restraint used the Penman-Monteith formulation (Liang et al., 2014) in SEBS (Su, 2002), removing the assumption that $\lambda E{=}AE$ at the cold and wet boundary. This makes SEBS-ER preferable for SEB applications in water limited environments (Zhang et al., 2008a).

The scene wide adjustment of T_S for the derivation of H_E within the first stage of the energy restraint does not compromise the information contained within the final SEBS-ER ET_a product. It is comparable to, and an extension of, the process with which satellite brightness temperature is atmospherically corrected to estimate T_S and the spatial detail/relationship between neighbouring land units is not compromised. Similarly, the second stage SHT analysis acts to globally stretch the distribution of H data between the limits of AE and H_{wet}, its execution is directly comparable to the CIMEC (calibration using inverse modeling at extreme conditions) process employed within METRIC and SEBAL (Allen et al., 2013).

Improved applicability of domain based calibration techniques are dependent on scales of implementation (Long and Singh, 2013). Platform dependent scale dependencies (McCabe and Wood, 2006) are critical for further deployment of the SEBS-ER model as domain and resolution dependencies can lead to mean absolute percentage difference (MAPD) in Λ of up to 50% (Long et al., 2012). Additionally, the ability to define the boundary pixels at

coarse scales (>250 m) becomes difficult within triangular ET_a frameworks (Zhang et al., 2008b) although, while the boundaries of the triangular framework may shift with domain size, the underlying spatial pattern remains consistent (Tian et al., 2013). Ultimately, these domain and scale based dependencies need to be addressed and tested before SEBS-ER can be confidently operated outside of the domain and scale of a 30 m Landsat tile.

A distinct difference between SEBS and SEBS-ER relates to the appropriate identification of clean and uncontaminated vegetated land units within the multispectral image scene. While SEBS does not rely on the surrounding 30 x 30 m land units (Su, 2002), SEBS-ER needs these surrounding units to define the limiting boundaries, SHR_{MIN} and SHR_{MAX}. Thus, inaccurate identification and masking of cloud, cloud shadow, snow cover, water bodies, sensor anomalies, urban areas, and steep terrain will likely alter the scene-wide distribution of T_S, creating bias within the derivation of SHR_{MIN} and SHR_{MAX} that will reduce accuracy within SEBS-ER ET_a estimates. Also, SEBS-ER would be particularly sensitive if cloud contaminated an area strongly representative of either the wet or dry edge of the SHT (Long et al., 2012), biasing λE values, increasing positively if the cold and wet edge (SHR_{MIN}) were obscured and increasing negatively if the hot and dry edge (SHR_{MAX}) were obscured. Further complicating analyses, not all SEB applications focus on areas equivalent to that of a Landsat image tile (approx 185 km x 185 km) (Evett et al., 2012; Long et al., 2012). Within the developed SEBS-ER energy restraint, the image processing constants derived for the identification of the upper and lower boundaries for SHR were manually optimised to suit the domain size and pixel resolution for that of a Landsat scene with between 0 and 30 percent cloud contamination and no Landsat 7 striping effects. While capability to specify a region of interest or employ SEBS-ER with alternative sensors requires alteration of the current SEBS-ER image search function (Fig 4), this would be a practical addition to the currently static SEBS-ER framework, enabling the production of more targeted and localised SEB products.

6.2. Sensitivity of SEBS and SEBS-ER to input error

SEBS-ER has improved stability and resilience, compared to SEBS, in its estimation of λE when we perturbed remotely sensed and meteorological inputs. The most substantial sensitivity reduction was for temperature inputs, T_S and T_A. This was important because there is substantial uncertainty in their estimation (Li et al., 2013; McVicar et al., 2007), particularly in heterogeneous landscapes (Vanwalleghem and Meentemeyer, 2009). Also, T_S and T_A are key inputs to the estimation of H and λE in SEBS and SEBS-ER, causing in-

teraction and exaggeration of their individual sensitivities (Yang and Shang, 2013). Overall, the reduced sensitivity of SEBS-ER is useful, improving resilience in estimated SEB fluxes from input errors and bias. Furthermore, SEBS-ER provided a more spatially uniform sensitivity response to each of the six remotely sensed and meteorological inputs, removing the variation in errors associated with landscape heterogeneity created by varying vegetation height and type (Kalma et al., 2008; Su, 2002; Timmermans et al., 2013).

Our sensitivity analysis for SEBS was consistent with Webster et al. (2016), with a strong sensitivity to T_S, T_A, and δ and weak sensitivity to P_{vap} (Fig. 6). The sensitivity to U_x was comparatively weaker among inputs compared to Webster et al. (2016) but is likely the result of individual land unit input perturbation rather than distinct scene-wide 2 standard deviation input shifts. Our analysis contrasted the SEBS meteorological sensitivity analyses conducted by Elhag (2016) where there was a significant effect for relative humidity, strongly associated with P_{vap}. Overall, the reduction in sensitivity exhibited by SEBS-ER was attributed to the mitigating effect of the domain based energy restraint from the collection of 30 x 30 m land units throughout the Landsat scene. This effect contrasted the direct approach inherent in SEBS, where the derivation of λE was specific and isolated to each 30 x 30 m land unit (Su, 2002). This also explained the residual λE variation in the sensitivity distribution plots (Fig. 6), another important point of difference between SEBS and SEBS-ER in this study. SEBS applications are affected by input error and bias for a selected area of interest, while SEBS-ER applications are affected by input error and bias for the entire Landsat scene. This reinforces the importance of confirming SEBS-ER's utility over alternative domains and spatial resolutions than that of a multispectral Landsat 5 or 7 product.

6.3. Validation and Performance of SEBS and SEBS-ER

SEBS-ER reduced the RMSE of λE estimates compared to SEBS, HTEM, and S-SEBI surface energy balance algorithms, when compared to two independent eddy covariance flux towers (Table 2). Also, among all flux tower comparisons, SEBS-ER showed a significant improvement compared to SEBS in λE accuracy (Table 3). The difference in the λE estimates at Tumbarumba were noticeably smaller and more consistent with SEBS-ER compared to SEBS (Fig. 8 and Table 2), particularly for a forested area with a 40 m canopy (Leuning, 2002). Furthermore, the underestimation of λE by SEBS-ER on the 1 Sep 2007 was likely attributed to the high density of land units along the cold and wet edge of the SHT density plot, caused from variation within R_{AH} data and the confounding effect of widespread snow

cover within the alpine areas of the Canberra study area (Fig. 1). Within SEBS-ER, these sharp and distinct changes in land type and their subsequent influence on T_S may also lead to discontinuities and separations within the SHT, preventing the image search algorithm from correctly identifying SHR_{min} and SHR_{max}. Similarly, the choice of interpolation method for U_x should be strongly considered, given its strong variability and influential effect on SHR through SEBS R_{AH} and H (Webster et al., 2016). This consideration of T_S and U_x discontinuities is an added complexity of SEBS-ER that is not currently required by SEBS (Su, 2002). Further development and validation is required if SEBS-ER is to be applied among land types other than the wet sclerophyll forest (van Gorsel et al., 2013) and sub alpine grassland assessed in this study (Leuning, 2002).

The low RMSE of SEBS-ER at the Nimmo High Plains flux tower was very positive (Table 2), given it relied on all land units within the Landsat scene for the energy restraint and that these land units were masked by cloud contamination, affected by topographic influences (McVicar et al., 2007; Webster et al., 2016), and representative of heterogeneous land covers and vegetation heights (Webster et al., 2016). The 32.2 $W\,m^{-2}$ RMSE of SEBS-ER at the sub-alpine grassland flux tower was less than that reported by Su et al. (2007) (61 $W\,m^{-2}$) for grassland and needle-leaf forest sites, less than that reported by Su et al. (2005) for maize and soybean (51 $W\,m^{-2}$), and less than that reported by Yang et al. (2010) in maize (80 $W\,m^{-2}$) and wheat (51 $W\,m^{-2}$). Limited to the comparison of the two flux towers, SEBS-ER had higher accuracy in λE estimates, compared to those obtained from SEBS in this study and others.

6.4. Temporal Stability of SEBS and SEBS-ER

SEBS-ER also had improved temporal stability compared to SEBS, reflected in reduced RMSE across land types and seasons, compared to an independent daily PT-JPL dataset (Fig. 10). Overall, the SEBS algorithm underestimated H as a result of inaccuracies and limitations within the derivation of the T_A, T_S, and R_{AH} spatial grids. These limitations resulted in an overestimation of λE which led to larger ET_a values than modelled by PT-JPL. SEBS-ER's scaling of sensible heat flux between AE and the wet limit (H_{wet}) ensured that it was fitted to the range of available energies within the domain of land units present in the Landsat scene, leading to reduced λE and ET_a estimations, more equivalent to those from PT-JPL. The scaling of H by SEBS-ER was also attributed to the more favourable comparison to pan evaporation data (Fig. 11), where the SEBS-ER algorithm substantially reduced the overestimation of ET_a over pan evaporation by SEBS, particular for smaller ET_a

estimates.

Increased temporal stability is an important factor in the estimation and application of ET_a estimates (Baldocchi et al., 2001; Senay et al., 2011), particularly for hydrological modelling in water catchment areas (Immerzeel and Droogers, 2008). Additionally, current downscaling techniques (Hong et al., 2011; Singh et al., 2014) continue to open opportunities for fusions between low spatial resolution, high temporal resolution data and high spatial resolution, low temporal resolution data (Singh et al., 2014). The improvement in temporal stability in SEBS-ER, over SEBS (Fig. 10 and Fig. 11), suggests that SEBS-ER would provide more reliable high temporal and spatial estimates of ET_a from such fused datasets. This would considerably help hydrological modelling and accounting in water catchment areas (Immerzeel and Droogers, 2008).

7. Conclusion

The integration of a domain based triangular energy restraint into the SEBS surface energy balance algorithm (Su, 2002) was successful over two heterogeneous study areas in south-east Australia. The new approach, SEBS-ER, effectively produced surface energy balance flux components and ET_a estimates with improved resilience to input error, significantly improved accuracy to flux tower references, and improved temporal stability, compared to daily PT-JPL data and pan evaporation measures. The SEBS-ER approach still needs to be tested in other ecosystems, across different geographic domains, and at different spatial scales, particularly in environments where the number of Landsat land units representative of extreme hot and dry or cold and wet conditions are relatively small. These current limitations arise because the SEBS-ER triangular search and energy restraint is static and does not respond to varying numbers of land units on either edge of the SHT or adapt to alternative geographic domains and sensor resolutions.

The added triangular energy restraint is novel in its use of surface energy balance flux components and the limitation imposed by H_{wet} to constrain H and λE using SHR. Further, SEBS-ER can largely mitigate the complex errors and uncertainties within remotely sensed, meteorological, and land type inputs to produce more reliable and accurate spatially distributed ET_a products. Continued improvements to the accuracy and reliability of exiting SEB algorithms, demonstrated by SEBS-ER, are a valuable contribution towards future research and the practical measurement of spatially distributed ET_a, particularly given the continued investment and commitment in medium resolution multispectral satellite platforms

with thermal infrared (Landsat 8, Landsat 9, Sentinel-3).

Acknowledgments

We thank the Sydney Catchment Authority, particularly Alan Benson for his coordination, for supporting this research through an Australian Research Council Linkage Grant (LP0990137). This work was supported by the Centre for Ecosystem Science, UNSW Australia. Landsat Surface Reflectance products were provided courtesy of the U.S. Geological Survey Earth Resources Observation and Science Center. We would also like to thank the Editor and four anonymous reviewers for their feedback, which substantially improved the manuscript.

References

Agam, N., Kustas, W. P., Anderson, M. C., Li, F., and Neale, C. M. (2007). A vegetation index based technique for spatial sharpening of thermal imagery. *Remote Sensing of Environment*, 107(4):545–558.

Allen, R., Irmak, A., Trezza, R., Hendrickx, J. M., Bastiaanssen, W., and Kjaersgaard, J. (2011a). Satellite-based et estimation in agriculture using SEBAL and METRIC. *Hydrological Processes*, 25(26):4011–4027.

Allen, R. G., Burnett, B., Kramber, W., Huntington, J., Kjaersgaard, J., Kilic, A., Kelly, C., and Trezza, R. (2013). Automated calibration of the METRIC-Landsat evapotranspiration process. *JAWRA Journal of the American Water Resources Association*, 49(3):563–576.

Allen, R. G., Pereira, L. S., Howell, T. A., and Jensen, M. E. (2011b). Evapotranspiration information reporting: I. factors governing measurement accuracy. *Agricultural Water Management*, 98(6):899–920.

Allen, R. G., Pereira, L. S., Raes, D., Smith, M., et al. (1998). Crop evapotranspiration-guidelines for computing crop water requirements-fao irrigation and drainage paper 56. *FAO, Rome*, 300(9):D05109.

Allen, R. G., Tasumi, M., and Trezza, R. (2007). Satellite-based energy balance for mapping evapotranspiration with internalized calibration (METRIC) - Model. *Journal of irrigation and drainage engineering*, 133(4):380–394.

692 Anderson, M. C., Allen, R. G., Morse, A., and Kustas, W. P. (2012). Use of landsat thermal
693 imagery in monitoring evapotranspiration and managing water resources. *Remote Sensing*
694 *of Environment*, 122:50–65.

695 Baldocchi, D., Falge, E., Gu, L., Olson, R., et al. (2001). Fluxnet: A new tool to study
696 the temporal and spatial variability of ecosystem-scale carbon dioxide, water vapor, and
697 energy flux densities. *Bulletin of the American Meteorological Society*, 82(11):2415.

698 Bastiaanssen, W., Menenti, M., Feddes, R., and Holtslag, A. (1998). A remote sensing
699 surface energy balance algorithm for land (sebal). 1. formulation. *Journal of hydrology*,
700 212:198–212.

701 Berk, A., Anderson, G. P., Bernstein, L. S., Acharya, P. K., Dothe, H., Matthew, M. W.,
702 Adler-Golden, S. M., Chetwynd Jr, J. H., Richtsmeier, S. C., Pukall, B., et al. (1999).
703 MODTRAN4 radiative transfer modeling for atmospheric correction. In *SPIE's Interna-*
704 *tional Symposium on Optical Science, Engineering, and Instrumentation*, pages 348–353.
705 International Society for Optics and Photonics.

706 Brutsaert, W. (1999). Aspects of bulk atmospheric boundary layer similarity under free-
707 convective conditions. *Reviews of geophysics*, 37(4):439–451.

708 Carlson, T. (2007). An overview of the" triangle method" for estimating surface evapotran-
709 spiration and soil moisture from satellite imagery. *Sensors*, 7(8):1612–1629.

710 Carlson, T. N. (1986). Regional-scale estimates of surface moisture availability and thermal
711 inertia using remote thermal measurements. *Remote Sensing Reviews*, 1(2):197–247.

712 Cesaraccio, C., Spano, D., Duce, P., and Snyder, R. L. (2001). An improved model for
713 determining degree-day values from daily temperature data. *International Journal of*
714 *Biometeorology*, 45(4):161–169.

715 Chen, Y., Xia, J., Liang, S., Feng, J., Fisher, J. B., Li, X., Li, X., Liu, S., Ma, Z., Miyata,
716 A., et al. (2014). Comparison of satellite-based evapotranspiration models over terrestrial
717 ecosystems in China. *Remote Sensing of Environment*, 140:279–293.

718 Chiew, F. H. S. and McMahon, T. A. (2002). Modelling the impacts of climate change on
719 australian streamflow. *Hydrological Processes*, 16(6):1235–1245.

Daly, C. (2006). Guidelines for assessing the suitability of spatial climate data sets. *International journal of climatology*, 26(6):707–721.

Donlon, C., Berruti, B., Buongiorno, A., Ferreira, M.-H., Féménias, P., Frerick, J., Goryl, P., Klein, U., Laur, H., Mavrocordatos, C., et al. (2012). The global monitoring for environment and security (GMES) sentinel-3 mission. *Remote Sensing of Environment*, 120:37–57.

Elhaddad, A. and Garcia, L. A. (2014). Using a surface energy balance model (ReSET-Raster) to estimate seasonal crop water use for large agricultural areas: Case study of the Palo Verde irrigation district. *Journal of Irrigation and Drainage Engineering*, 140(10).

Elhag, M. (2016). Inconsistencies of sebs model output based on the model inputs: Global sensitivity contemplations. *Journal of the Indian Society of Remote Sensing*, pages 1–8.

Evett, S. R., Kustas, W. P., Gowda, P. H., Anderson, M. C., Prueger, J. H., and Howell, T. A. (2012). Overview of the Bushland Evapotranspiration and Agricultural Remote sensing EXperiment 2008 (BEAREX08): A field experiment evaluating methods for quantifying ET at multiple scales. *Advances in Water Resources*, 50:4–19.

Fisher, J. B., Tu, K. P., and Baldocchi, D. D. (2008). Global estimates of the land–atmosphere water flux based on monthly avhrr and islscp-ii data, validated at 16 fluxnet sites. *Remote Sensing of Environment*, 112(3):901–919.

Gallant, J., Dowling, T., Read, A., Wilson, N., and Tickle, P. (2011). 1 second SRTM Level 2 Derived Smoothed Digital Elevation Model (DEM-S) Version 1. Technical report, Geoscience Australia, Canberra.

Gampe, D., Ludwig, R., Qahman, K., and Afifi, S. (2016). Applying the Triangle Method for the parameterization of irrigated areas as input for spatially distributed hydrological modelingAssessing future drought risk in the Gaza Strip (Palestine). *Science of The Total Environment*, 543:877–888.

Garratt, J. and Hicks, B. (1973). Momentum, heat and water vapour transfer to and from natural and artificial surfaces. *Quarterly Journal of the Royal Meteorological Society*, 99(422):680–687.

748 Gibson, L., Münch, Z., and Engelbrecht, J. (2011). Particular uncertainties encountered in
749 using a pre-packaged SEBS model to derive evapotranspiration in a heterogeneous study
750 area in South Africa. *Hydrology and Earth System Sciences*, 15(1):295–310.

751 Glenn, E. P., Doody, T. M., Guerschman, J. P., Huete, A. R., King, E. A., McVicar, T. R.,
752 Van Dijk, A. I., Van Niel, T. G., Yebra, M., and Zhang, Y. (2011). Actual evapotran-
753 spiration estimation by ground and remote sensing methods: the australian experience.
754 *Hydrological Processes*, 25(26):4103–4116.

755 Gokmen, M., Vekerdy, Z., Verhoef, A., Verhoef, W., Batelaan, O., and van der Tol, C.
756 (2012). Integration of soil moisture in SEBS for improving evapotranspiration estimation
757 under water stress conditions. *Remote Sensing of Environment*, 121:261 – 274.

758 Han, L., Wang, P., Yang, H., Liu, S., and Wang, J. (2006). Study on ndvi-t s space by
759 combining lai and evapotranspiration. *Science in China Series D*, 49(7):747–754.

760 Hong, S.-h., Hendrickx, J. M., and Borchers, B. (2011). Down-scaling of sebal derived
761 evapotranspiration maps from modis (250 m) to landsat (30 m) scales. *International*
762 *journal of remote sensing*, 32(21):6457–6477.

763 Huete, A., Didan, K., Miura, T., Rodriguez, E. P., Gao, X., and Ferreira, L. G. (2002).
764 Overview of the radiometric and biophysical performance of the modis vegetation indices.
765 *Remote sensing of environment*, 83(1):195–213.

766 Immerzeel, W. and Droogers, P. (2008). Calibration of a distributed hydrological model
767 based on satellite evapotranspiration. *Journal of Hydrology*, 349(3):411–424.

768 Jones, E., Oliphant, T., and Peterson, P. (2014). SciPy: Open source scientific tools for
769 Python. Technical report, Scipy.org.

770 Kalma, J. D., McVicar, T. R., and McCabe, M. F. (2008). Estimating land surface evapo-
771 ration: A review of methods using remotely sensed surface temperature data. *Surveys in*
772 *Geophysics*, 29(4-5):421–469.

773 Keith, D. A. (2004). *Ocean shores to desert dunes: the native vegetation of NSW and the*
774 *ACT (Selected Extracts)*. Department of Environment and Conservation (NSW).

Knipper, K. R., Kinoshita, A. M., and Hogue, T. S. (2016). Evaluation of a moderate resolution imaging spectroradiometer triangle-based algorithm for evapotranspiration estimates in subalpine regions. *Journal of Applied Remote Sensing*, 10(1):016002–016002.

Kustas, W. P. and Norman, J. M. (1997). A two-source approach for estimating turbulent fluxes using multiple angle thermal infrared observations. *Water Resources Research*, 33(6):1495–1508.

Leuning, R. (2002). Ozflux: An integrated program to study cycles of water and carbon in australian terrestrial systems/leuning r., et al. In *Proc. 2nd Intern. Workshop on Advanced Flux Network and Flux Evaluation, Jeju, AsiaF-lux*, page 5.

Li, Z.-L., Tang, B.-H., Wu, H., Ren, H., Yan, G., Wan, Z., Trigo, I. F., and Sobrino, J. A. (2013). Satellite-derived land surface temperature: Current status and perspectives. *Remote Sensing of Environment*, 131:14 – 37.

Lian, J. and Huang, M. (2016). Comparison of three remote sensing based models to estimate evapotranspiration in an oasis-desert region. *Agricultural Water Management*, 165:153–162.

Liang, S., Zhongxin, C., and Zhiwei, J. (2014). Estimation of regional evapotranspiration over the southern great plains based on penman-monteith theory and the soil moisture estimates. In *Agro-geoinformatics (Agro-geoinformatics 2014), Third International Conference on*, pages 1–5. IEEE.

Liaqat, U. W. and Choi, M. (2015). Surface energy fluxes in the northeast Asia ecosystem: SEBS and METRIC models using Landsat satellite images. *Agricultural and Forest Meteorology*, 214215:60 – 79.

Long, D. and Singh, V. P. (2012). A two-source trapezoid model for evapotranspiration (ttme) from satellite imagery. *Remote Sensing of Environment*, 121:370–388.

Long, D. and Singh, V. P. (2013). Assessing the impact of end-member selection on the accuracy of satellite-based spatial variability models for actual evapotranspiration estimation. *Water Resources Research*, 49(5):2601–2618.

Long, D., Singh, V. P., and Scanlon, B. R. (2012). Deriving theoretical boundaries to address scale dependencies of triangle models for evapotranspiration estimation. *Journal of Geophysical Research: Atmospheres*, 117(D5).

Masek, J., Vermote, E., Saleous, N., Wolfe, R., Hall, F., Huemmrich, K., Gao, F., Kutler, J., and Lim, T.-K. (2006). A landsat surface reflectance dataset for north america, 1990-2000. *Geoscience and Remote Sensing Letters, IEEE*, 3(1):68–72.

McCabe, M. F. and Wood, E. F. (2006). Scale influences on the remote estimation of evapotranspiration using multiple satellite sensors. *Remote Sensing of Environment*, 105(4):271–285.

McMahon, T., Peel, M., Lowe, L., Srikanthan, R., and McVicar, T. (2013). Estimating actual, potential, reference crop and pan evaporation using standard meteorological data: a pragmatic synthesis. *Hydrology and Earth System Sciences*, 17(4):1331–1363.

McVicar, T. R., Roderick, M. L., Donohue, R. J., Li, L. T., Van Niel, T. G., Thomas, A., Grieser, J., Jhajharia, D., Himri, Y., Mahowald, N. M., et al. (2012). Global review and synthesis of trends in observed terrestrial near-surface wind speeds: Implications for evaporation. *Journal of Hydrology*, 416:182–205.

McVicar, T. R., Van Niel, T. G., Li, L., Hutchinson, M. F., Mu, X., and Liu, Z. (2007). Spatially distributing monthly reference evapotranspiration and pan evaporation considering topographic influences. *Journal of hydrology*, 338(3):196–220.

Merz, R., Parajka, J., and Blöschl, G. (2011). Time stability of catchment model parameters: Implications for climate impact analyses. *Water Resources Research*, 47(2).

Monteith, J. L., editor (1965). *Evaporation and environment*, volume 19 of *205-23*.

Mu, Q., Zhao, M., and Running, S. W. (2011). Improvements to a modis global terrestrial evapotranspiration algorithm. *Remote Sensing of Environment*, 115(8):1781–1800.

Petropoulos, G., Carlson, T. N., and Wooster, M. J. (2009a). An overview of the use of the simsphere soil vegetation atmosphere transfer (SVAT) model for the study of land-atmosphere interactions. *Sensors*, 9(6):4286–4308.

Petropoulos, G., Wooster, M., Carlson, T., Kennedy, M., and Scholze, M. (2009b). A global bayesian sensitivity analysis of the 1d simsphere soil–vegetation–atmospheric transfer (SVAT) model using gaussian model emulation. *Ecological Modelling*, 220(19):2427–2440.

Price, J. C. (1990). Using spatial context in satellite data to infer regional scale evapotranspiration. *Geoscience and Remote Sensing, IEEE Transactions on*, 28(5):940–948.

Priestley, C. and Taylor, R. (1972). On the assessment of surface heat flux and evaporation using large-scale parameters. *Monthly weather review*, 100(2):81–92.

Roerink, G., Su, Z., and Menenti, M. (2000). S-sebi: A simple remote sensing algorithm to estimate the surface energy balance. *Physics and Chemistry of the Earth, Part B: Hydrology, Oceans and Atmosphere*, 25(2):147 – 157.

Roy, D., Wulder, M., Loveland, T., C.E., W., Allen, R., Anderson, M., Helder, D., Irons, J., Johnson, D., Kennedy, R., Scambos, T., Schaaf, C., Schott, J., Sheng, Y., Vermote, E., Belward, A., Bindschadler, R., Cohen, W., Gao, F., Hipple, J., Hostert, P., Huntington, J., Justice, C., Kilic, A., Kovalskyy, V., Lee, Z., Lymburner, L., Masek, J., McCorkel, J., Shuai, Y., Trezza, R., Vogelmann, J., Wynne, R., and Zhu, Z. (2014). Landsat-8: Science and product vision for terrestrial global change research. *Remote Sensing of Environment*, 145:154 – 172.

Rwasoka, D., Gumindoga, W., and Gwenzi, J. (2011). Estimation of actual evapotranspiration using the Surface Energy Balance System (SEBS) algorithm in the Upper Manyame catchment in Zimbabwe. *Physics and Chemistry of the Earth, Parts A/B/C*, 36(14):736–746.

Scarth, P. (2014). Continental scale forest and woodland structure mapping using landsat, alos palsar and glas icesat. In *ForestSAT2014 Open Conference System*.

Scarth, P., Phinn, S., and McAlpine, C. (2001). Integrating high and moderate spatial resolution image data to estimate forest age structure. *Canadian Journal of Remote Sensing*, 27(2):129–142.

Senay, G. B., Budde, M. E., and Verdin, J. P. (2011). Enhancing the simplified surface energy balance (SSEB) approach for estimating landscape et: Validation with the metric model. *Agricultural Water Management*, 98(4):606–618.

Simpson, R. (2012). Nimmo high plains ozflux tower site ozflux: Australian and new zealand flux research and monitoring. hdl: 102.100.100/14220.

Singh, R. K., Senay, G. B., Velpuri, N. M., Bohms, S., and Verdin, J. P. (2014). On the downscaling of actual evapotranspiration maps based on combination of modis and landsat-based actual evapotranspiration estimates. *Remote Sensing*, 6(11):10483–10509.

Su, H., McCabe, M., Wood, E., Su, Z., and Prueger, J. (2005). Modeling evapotranspiration during smacex: Comparing two approaches for local-and regional-scale prediction. *Journal of hydrometeorology*, 6(6):910–922.

Su, H., Wood, E., McCabe, M., and Su, Z. (2007). Evaluation of remotely sensed evapotranspiration over the ceop eop-1 reference sites. *Meteorological society of Japan*, 85:439–459.

Su, Z. (2002). The surface energy balance system (sebs) for estimation of turbulent heat fluxes. *Hydrology and Earth System Sciences Discussions*, 6(1):85–100.

Sun, H. (2016). Two-stage trapezoid: A new interpretation of the land surface temperature and fractional vegetation coverage space. *IEEE JOURNAL OF SELECTED TOPICS IN APPLIED EARTH OBSERVATIONS AND REMOTE SENSING*, 9(1):336–346.

Tang, R., Li, Z.-L., Jia, Y., Li, C., Sun, X., Kustas, W. P., and Anderson, M. C. (2011). An intercomparison of three remote sensing-based energy balance models using large aperture scintillometer measurements over a wheat–corn production region. *Remote Sensing of Environment*, 115(12):3187–3202.

Tang, R., Li, Z.-L., and Tang, B. (2010). An application of the t s–vi triangle method with enhanced edges determination for evapotranspiration estimation from modis data in arid and semi-arid regions: Implementation and validation. *Remote Sensing of Environment*, 114(3):540–551.

Tian, J., Su, H., Sun, X., Chen, S., He, H., and Zhao, L. (2013). Impact of the spatial domain size on the performance of the ts-vi triangle method in terrestrial evapotranspiration estimation. *Remote Sensing*, 5(4):1998–2013.

Timmermans, J., Su, Z., Tol, C., Verhoef, A., and Verhoef, W. (2013). Quantifying the uncertainty in estimates of surface–atmosphere fluxes through joint evaluation of the sebs and scope models. *Hydrology and earth system sciences*, 17(4):1561–1573.

USGS, L. D. (2009). MOD13Q1. *USGS/Earth Resources Observation and Science (EROS) Center, Sioux Falls, South Dakota*.

van Gorsel, E., Berni, J., Briggs, P., Cabello-Leblic, A., Chasmer, L., Cleugh, H., Hacker, J., Hantson, S., Haverd, V., Hughes, D., and et al. (2013). Primary and secondary effects of climate variability on net ecosystem carbon exchange in an evergreen eucalyptus forest. *Agricultural and Forest Meteorology*, 182183:248 – 256.

Van Niel, T. G., McVicar, T. R., Roderick, M. L., van Dijk, A. I., Beringer, J., Hutley, L. B., and Van Gorsel, E. (2012). Upscaling latent heat flux for thermal remote sensing studies: Comparison of alternative approaches and correction of bias. *Journal of Hydrology*, 468:35–46.

Van Niel, T. G., McVicar, T. R., Roderick, M. L., van Dijk, A. I., Renzullo, L. J., and Van Gorsel, E. (2011). Correcting for systematic error in satellite-derived latent heat flux due to assumptions in temporal scaling: Assessment from flux tower observations. *Journal of Hydrology*, 409(1):140–148.

Vanwalleghem, T. and Meentemeyer, R. (2009). Predicting forest microclimate in heterogeneous landscapes. *Ecosystems*, 12(7):1158–1172.

Wang, X.-G., Wang, W., Huang, D., Yong, B., and Chen, X. (2014). Modifying sebal model based on the trapezoidal relationship between land surface temperature and vegetation index for actual evapotranspiration estimation. *Remote Sensing*, 6(7):5909.

Webster, E., Ramp, D., and Kingsford, R. T. (2016). Spatial sensitivity of surface energy balance algorithms to meteorological data in a heterogeneous environment. *Remote Sensing of Environment*, 187:294 – 319.

Winsemius, H., Schaefli, B., Montanari, A., and Savenije, H. (2009). On the calibration of hydrological models in ungauged basins: A framework for integrating hard and soft hydrological information. *Water Resources Research*, 45(12).

Yang, D., Chen, H., and Lei, H. (2010). Estimation of evapotranspiration using a remote sensing model over agricultural land in the north china plain. *International Journal of Remote Sensing*, 31(14):3783–3798.

Yang, Y. and Shang, S. (2013). A hybrid dual-source scheme and trapezoid framework–based evapotranspiration model (HTEM) using satellite images: Algorithm and model test. *Journal of Geophysical Research: Atmospheres*, 118(5):2284–2300.

Yao, Y., Liang, S., Cheng, J., Liu, S., Fisher, J. B., Zhang, X., Jia, K., Zhao, X., Qin, Q., Zhao, B., et al. (2013). Modis-driven estimation of terrestrial latent heat flux in china based on a modified priestley–taylor algorithm. *Agricultural and forest meteorology*, 171:187–202.

Yin, J., Zhan, C., Wang, H., and Wang, F. (2016). Integration of remote sensing evapotranspiration (et) model and hydrologic model for mapping daily et time-series at river basin scale. *Hydrology Research*, page nh2016165.

Zhang, L., Potter, N., Hickel, K., Zhang, Y., and Shao, Q. (2008a). Water balance modeling over variable time scales based on the budyko framework–model development and testing. *Journal of Hydrology*, 360(1):117–131.

Zhang, R., Tian, J., Su, H., Sun, X., Chen, S., and Xia, J. (2008b). Two improvements of an operational two-layer model for terrestrial surface heat flux retrieval. *Sensors*, 8(10):6165–6187.

Appendix A

A.1. Data sources and preprocessing

Atmospherically corrected shortwave Landsat data were obtained from the United States Geological Survey (USGS) Earth Resources Observation and Science (EROS) Center Science Processing Architecture On Demand Interface (EPSG) (espa.cr.usgs.gov). These data consisted of visible and near infrared surface reflectance bands, a thermal radiance band, and precalculated vegetation indices (Masek et al., 2006). Landsat thermal data was atmospherically corrected using MODTRAN model (Berk et al., 1999), narrowband transmissivity, path radiance, and sky radiance values are listed for each Landsat acquisition date in the Canberra (Table A1) and Sydney (Table A2) study areas. In addition to the Landsat data, Bureau of Meteorology (BOM) minimum temperature (T_M, $^{\circ}C$), maximum temperature (T_X, $^{\circ}C$), U_x, air pressure (P_{air}, kPa), P_{vap}, and δ data were collated for use from a spatial subset of BOM ground stations within a 100 km buffer of each respective study area (Fig. 1). U_x, P_{air}, and P_{vap} stations were additionally subset to those with at least six observations for the respective Landsat acquisition day. Elevation data were sourced from the shuttle radar topography mission (SRTM) (Gallant et al., 2011) and vegetation height data were obtained from a 2009 Australian dataset (Scarth et al., 2001) that combined ALOS-1 PALSAR, Landsat, and ICESat/GLAS data.

To complement the temporal (Fig. 2b) and spatial (Fig. 1) extent of the Landsat data in the Sydney study area, the MOD13Q1 product (USGS, 2009) from the Moderate Resolution Imaging Spectrometer (MODIS) were obtained for use in the PT-JPL algorithm (Fisher et al., 2008). Data was acquired from the USGS Land Processes Distributed Active Archive Center (LP DAAC) and the 250 m 16 day average Normalized Difference Vegetation Index (NDVI) images were extracted from the MOD13Q1 archive and reprojected to the UTM 55N map projection of the Landsat data. Daily BOM T_M, T_X, δ, P_{vap}, and P_{sat} data were also collated for use in the PT-JPL algorithm. Station data within a 100 km buffer of the Sydney study area (Fig. 1) were selected for use. P_{vap} and P_{sat} data were additionally subset to those stations with at least six observations for each respective day.

Table A1: Atmospheric correction parameters (Transmissivity τ_{NB}, Path Radiance R_P and Downwelling Radiance R_{SKY}) obtained using MODTRAN (Berk et al., 1999) for Landsat thermal data in the Canberra study area (Fig. 1).

Acquisition Date	τ_{NB}	R_P	R_{SKY}
17 Nov 2006	0.92	0.50	0.89
05 Feb 2007	0.78	1.68	2.74
09 Mar 2007	0.92	0.53	0.93
26 Apr 2007	0.93	0.43	0.75
12 May 2007	0.91	0.59	1.02
01 Sep 2007	0.95	0.27	0.49
16 Oct 2008	0.94	0.41	0.75
26 Apr 2001	0.88	0.86	1.49
29 Jun 2001	0.90	0.69	1.19

Table A2: Atmospheric correction parameters (Transmissivity τ_{NB}, Path Radiance R_P and Downwelling Radiance R_{SKY}) obtained using MODTRAN (Berk et al., 1999) for Landsat thermal data in the Sydney study area (Fig. 1).

Acquisition Date	τ_{NB}	R_P	R_{SKY}
01 Dec 1999	0.83	1.2	2.04
03 Feb 2000	0.83	1.31	2.23
09 May 2000	0.9	0.69	1.18
12 Jul 2000	0.95	0.33	0.58
14 Sep 2000	0.92	0.56	0.97
16 Oct 2000	0.91	0.55	0.96
26 Apr 2001	0.85	0.99	1.69
29 Jun 2001	0.9	0.64	1.08
31 Jul 2001	0.9	0.64	1.08
08 Feb 2002	0.75	1.82	2.97
12 Mar 2002	0.74	1.82	2.95
13 Apr 2002	0.81	1.42	2.34
16 Jun 2002	0.86	0.91	1.53
02 Jul 2002	0.93	0.46	0.78
18 Jul 2002	0.93	0.45	0.79
04 Sep 2002	0.89	0.76	1.3
22 Oct 2002	0.94	0.39	0.72
07 Nov 2002	0.94	0.45	0.82
26 Jan 2003	0.82	1.47	2.46
16 Apr 2003	0.93	0.48	0.83
13 Jul 2003	0.91	0.54	0.93
15 Sep 2003	0.91	0.52	0.9
04 Dec 2003	0.73	2.01	3.27
09 Mar 2004	0.74	1.96	3.19
29 Jun 2004	0.9	0.64	1.09
15 Jul 2004	0.91	0.54	0.92
31 Jul 2004	0.93	0.41	0.71
17 Sep 2004	0.9	0.68	1.16
03 Oct 2004	0.87	0.88	1.5
22 Dec 2004	0.85	1.11	1.92
07 Jan 2005	0.95	0.31	0.57
08 Feb 2005	0.8	1.41	2.42
24 Feb 2005	0.79	1.65	2.71
12 Mar 2005	0.84	1.28	2.13
18 Jul 2005	0.92	0.46	0.79
16 Apr 2006	0.93	0.45	0.78
05 Jul 2006	0.86	0.83	1.4
22 Aug 2006	0.92	0.51	0.88
23 Sep 2006	0.91	0.59	1.04
09 Oct 2006	0.96	0.24	0.45
10 Nov 2006	0.89	0.76	1.31
28 Dec 2006	0.83	1.25	2.12
29 Jan 2007	0.84	1.15	1.95
05 May 2007	0.86	0.98	1.63
22 Jun 2007	0.94	0.33	0.58
10 Sep 2007	0.88	0.76	1.32
04 Mar 2008	0.83	1.23	2.05
20 Mar 2008	0.81	1.44	2.39
28 Sep 2008	0.86	1.02	1.72
18 Jan 2009	0.87	0.96	1.64
21 Jan 2010	0.8	1.44	2.42
22 Feb 2010	0.69	2.39	3.82
26 Mar 2010	0.79	1.63	2.68

Appendix B

B.1. Sensible Heat Triangle image processing routine

To objectively identify the boundaries of the Sensible Heat Triangle (SHT), we first determined the domain range of the SHT using histograms of SHR and EVI to determine the horizontal (SHR_{1DMAX} and SHR_{1DMIN}) and vertical (EVI_{1DMAX} and EVI_{1DMIN}) limits of the subsequent two dimensional density SHT analysis. The SHT limits were determined where:

- SHR_{1DMIN} was the lower SHR where the bin count reached 1/15000 of the peak,
- SHR_{1DMAX} was the upper SHR where the bin count reached 1/30000 of the peak,
- EVI_{1DMIN} was the lower EVI where the bin count reached 1/5000 of the peak, and
- EVI_{1DMAX} was the upper EVI where the bin count reached 1/5000 of the peak.

The one dimensional density limits (SHR_{1DMIN}, SHR_{1DMAX}, EVI_{1DMIN} and EVI_{1DMAX}) were then used to produce the 2D SHT density distribution histogram, with 1200 SHR bins and 1000 EVI bins.

To isolate the horizontal and vertical limits of the SHT distribution, a nine cell 2D correlation filter (Jones et al., 2014) was then used to smooth and enhance the boundary of the density distribution. Then, a custom image search function was created to identify the horizontal and vertical edges of the SHT using an iterative search routine that emanated from the peak density point within the 2D SHT density distribution (Fig. 4). The boundary pixels were then used to identify the left (SHR_{MIN}), right (SHR_{MAX}), top (EVI_{MAX}) and bottom (EVI_{MIN}) edges of the triangular SHT domain (Fig. 4). Through manual optimisation, the boundaries of the SHT were identified where:

- EVI_{MIN} was the average of the lowest 48 boundary pixels,
- EVI_{MAX} was the average of the highest 12 boundary pixels,
- SHR_{MIN} was the average of the lowest 48 boundary pixels, and
- SHR_{MAX} was the average of the highest 12 boundary pixels.

The number of boundary pixels for each SHT limit were reflective of the number of horizontal and vertical bins used to construct the SHT (1200 x 1000), the expectant shape of the SHT density distribution (Fig. 4), and the relative domain and resolution of a Landsat tile with between 0 and 30 percent cloud contamination.

LIST OF FIGURE CAPTIONS

- Figure 1: Two study areas in south-east Australia: a) the Sydney study area (Landsat tile (path 90, row 84)) contained two long term pan evaporation stations (squares with station IDs); and b) the Canberra study area (Landsat tile (path 91, row 85)), with the Tumbarumba (star T) and Nimmo High Plains (star N) eddy covariance flux towers. Dark grey diamonds were the meteorological ground stations used to source T_A, U_x, P_{vap}, and P_{air} meteorological inputs for SEBS and SEBS-ER. The RS1 annotation indicates the location of the Wagga Wagga radiosonde station and the RS2 annotation indicates the location of the Sydney International airport radiosonde station. Coloured Shading showed relative height of the vegetation across south east Australia (Scarth, 2014). The WGS 84 coordinate grid was overlaid on top of the map UTM 55N projection.

- Figure 2: a) Nine Landsat acquisition dates for the Canberra study area (Fig. 1) were used to test the sensitivity, resilience and accuracy of the SEBS and SEBS-ER surface energy balance algorithms. All nine Landsat acquisitions were from the Landsat 5 Thematic Mapper (TM) (blue). b) Fifty-two Landsat acquisition dates for the Sydney study area (Fig. 1) were used to test the temporal stability of the SEBS and SEBS-ER surface energy balance algorithms. The Landsat data (1 Dec 1999 - 16 Apr 2003) were acquired by the Landsat 7 ETM+ (red) while Landsat data from 13 Jul 2003 onwards were acquired by the Landsat 5 TM (blue).Precise acquisition dates ca be found within the atmospheric correction tables located in Appendix A.

- Figure 3: A flowchart depicting the two stage energy restraint incorporated into the Surface Energy Balance System. The first stage (orange shaded area) quantifies a global offset for surface temperature, while the second stage (blue shaded area) uses a domain-based image search routine to identify the limits of the Sensible Heat Ratio (SHR) to make a gradient and offset correction to sensible heat flux (H). The routine continues until the aerodynamic resistance and the gradient and offset correction parameters stabilise.

- Figure 4: The constraint and adjustment of the SEBS-ER Sensible Heat Triangle (SHT), defined by SHR_{MAX} and SHR_{MIN} values and a gradient (A_{ER}) and intercept (B_{ER}) applied to adjust the input SHT distribution (shaded grey) to a new SHT with an SHR ranged between 0 and 1 (dark striped).

- Figure 5: Sensible Heat Triangles (SHT) showing the density distribution of the Sensible Heat Ratio (SHR) to the Enhanced Vegetation Index (Vegetation Fraction) for a) 17 Nov 2006, b) 5 Feb 2007, c) 9 Mar 2007, d) 26 Apr 2007, e) 12 May 2007, f) 1 Sep 2007, g) 8 Dec 2008, h) 25 Jan 2009 and j) 26 Feb 2009, where darker colours indicated higher densities. The horizontal dashed lines were the derived upper and lower limits of vegetation cover, while the vertical dashed lines represented the derived upper and lower limits of evaporative energy.

- Figure 6: Temporally averaged comparisons of λE input sensitivity for i) SEBS and ii) SEBS-ER surface energy balance algorithms after perturbing different input variables: a) surface temperature (T_S); b) air temperature (T_A); c) daily solar exposure (δ); d) surface roughness (Z_{OM}); e) wind speed (U_x); and f) vapour pressure (P_{vap}), where darker shading represented higher densities. Linear regressions between the change in λE to the % change of each input parameter were represented by dashed black lines, with the gradient coefficient (m) and R^2 statistic displayed at the top of each density plot.

- Figure 7: Temporally averaged spatial grids of λE sensitivity from perturbation in (i) SEBS and (ii) SEBS-ER input variables in the Canberra study area (black polygon). Grids show the relative spatial change in λE related to a 1% change in (a) surface temperature (T_S, $^{\circ}C$), (b) air temperature (T_A, $^{\circ}C$), (c) solar exposure (δ, $MJ\,day^{-1}$), (d) surface roughness for momentum (Z_{OM}, m), (e) wind speed (U_x, $m\,s{-}1$), and (f) vapour pressure (P_{vap}, kPa). Note the scale change between T_S, T_A and δ (0 - 7.5 $W\,m^{-2}$) and Z_{OM}, U_x and P_{vap} (0 - 2.5 $W\,m^{-2}$). UTM Eastings and Northings were for Zone 55 North.

- Figure 8: 750 m radial samples of λE ($W\,m^{-2}$) ($\pm$2 SD) from S-SEBI and HTEM (Webster et al., 2016) and SEBS and SEBS-ER, compared to λE observed at the Tumbarumba flux tower (black) (Fig. 1) for the nine acquisition dates: (a) 17 Nov 2006; (b) 5 Feb 2007; (c) 9 Mar 2007; (d) 26 Apr 2007; (e) 12 May 2007; (f) 1 Sep 2007; (g) 8 Dec 2008; (h) 25 Jan 2009; and (j) 26 Feb 2009.

- Figure 9: 30 m radial samples of λE ($W\,m^{-2}$) ($\pm$2 SD) from S-SEBI and HTEM (Webster et al., 2016) and SEBS and SEBS-ER, compared to λE observed at the Nimmo High Plains flux tower (black) (Fig. 1) for three acquisition dates: (c) 9 Mar 2007; (e) 12 May 2007; and (f) 1 Sep 2007.

- Figure 10: Multifaceted comparison of SEBS and SEBS-ER ET_a to daily PT-JPL ET_a data, showing the temporal average root mean square error (RMSE) spatially ($mmday^{-1}$) of (a) SEBS and (b) SEBS-ER and the comparisons of density distributions between PT-JPL ET_a to (c) SEBS ET_a and (d) SEBS-ER ET_a. Seasonal differences in SEBS and SEBS-ER ET_a, compared to PT-JPL ET_a were captured in estimates of mean absolute error (MAE), ($mm\,day^{-1}$) for acquisitions in (e) summer, (f) autumn, (g) winter, and (h) spring.

- Figure 11: Daily pan evaporation data ($mm\,day^{-1}$) from stations (x) 070014 and (+) 070263 in the Sydney study area (Fig. 1) over a ten year period (Fig. 2b) compared to actual evapotranspiration (ET_a, $mm\,day^{-1}$) from (a) SEBS and (b) SEBS-ER. The red shaded area indicates unrealistic estimates of SEBS and SEBS-ER ET_a and the green shaded area indicates valid SEBS and SEBS-ER ET_a estimates.